

Alma Mater Studiorum – Università di Bologna

DOTTORATO DI RICERCA IN
Meccanica e scienze avanzate dell'ingegneria

Ciclo XXVI

Settore Concorsuale di afferenza: 09/A2 - MECCANICA APPLICATA ALLE MACCHINE

Settore Scientifico disciplinare: ING-IND/13 - MECCANICA APPLICATA ALLE MACCHINE

Dynamic analysis of the motorcycle chattering behaviour by means of
symbolic multibody modelling.

Presentata da: **LUCA LEONELLI**

Coordinatore Dottorato

Relatore

Prof. V. Parenti Castelli

Prof. G. Catania

Esame finale anno 2014

SUMMARY

Nowadays rigid multibody modelling is a well-established technique for the analysis of stability and dynamic behaviour of road-racing motorcycles, reducing designing times and avoiding the risks and costs related to experimental testing. In order to provide accurate assessments of ride and handling performances a tire model capable of representing the dynamic response of rolling over uneven surfaces is required. While extensive research efforts have been dedicated to car tires, leading to the development of the so-called rigid-ring model, its application to motorcycles presents a number of issues.

Aim of this research is the development and validation of a comprehensive multibody motorcycle model featuring rigid-ring tires, taking into account both slope and roughness of road surfaces. A novel parametrization for the general kinematics of the motorcycle is proposed, using a mixed reference-point and relative-coordinates approach. The resulting description, developed in terms of dependent coordinates, makes it possible to efficiently include rigid-ring kinematics as well as road elevation and slope. The equations of motion for the multibody system are derived symbolically and the constraint equations arising from the dependent-coordinate formulation are handled using a projection technique. Therefore the resulting system of equations can be integrated in time domain using a standard ODE algorithm.

The model is validated with respect to maneuvers experimentally measured on the race track, showing consistent results and excellent computational efficiency. More in detail, it is also capable of reproducing the chatter vibration of racing motorcycles. The chatter phenomenon, appearing during high speed cornering maneuvers, consists of a self-excited vertical oscillation of both the front and rear unsprung masses in the range of frequency between 17 and 22 Hz. A critical maneuver is numerically simulated, and a self-excited vibration appears, consistent with the experimentally measured chatter vibration. Finally, the driving mechanism for the self-excitation is highlighted and a physical interpretation is proposed.

ACKNOWLEDGMENTS

The author wishes to express his gratitude to Prof. Silvio Sorrentino (University of Modena and Reggio Emilia) for the invaluable help during the development of this thesis.

The support from engineers Nicolò Mancinelli, Marco Amorosa and Roberto Costa of Ducati Motor Holding, Ducati Corse Division is also kindly acknowledged.

CONTENTS

- Chapter 1: Motorcycle model	1
- 1.1 Introduction	2
- 1.2 Motorcycle model geometry	4
- 1.3 Rigid-ring tire model	8
- 1.4 Transmission model	13
- 1.5 Derivation of the equations of motion	16
- 1.6 Model summary	22
- 1.7 Conclusions	25
- Chapter 2: Shock absorber model	27
- 2.1 Introduction	28
- 2.2 Planar motorcycle model	29
- 2.3 Shock absorber model	32
- 2.4 Ground roughness model	37
- 2.5 Two different maneuvers	39
- 2.6 Optimization objective function	30
- 2.7 Optimization results	42
- 2.8 Conclusions	44
- Chapter 3: A simplified planar model for the analysis of motorcycle chatter	45
- 3.1 Introduction	46
- 3.2 Planar model	46
- 3.3 Stability analysis	50
- 3.4 Remark on slip models	54
- 3.5 Conclusions	58
- Chapter 4: The chattering vibration of racing motorcycles	59
- 4.1 Introduction	60
- 4.2 Parameter estimation	61
- 4.3 Maneuver description	62
- 4.4 Model linearization	65
- 4.5 Maneuver simulation	68
- 4.6 Conclusions	71
- References	75

Chapter 1

MOTORCYCLE MODEL

1.1 INTRODUCTION

Several motorcycle models have been presented in the literature, showing a very good agreement with experimental data for a wide range of maneuvers. Several dedicated commercial softwares are available as well, though their computational efficiency is usually lower in comparison with purposely built codes.

Main contributions on multibody motorcycle modelling include the works of Cossalter [1] and Sharp [2], [3]. Both authors developed advanced tridimensional, rigid multibody models of motorcycles with standard geometry (namely front telescopic forks and rear oscillating swingarm suspensions), featuring chain transmissions, torus-shaped tires and empirical models of tire-ground interaction forces (Magic Formula, MF), making it possible to take into account the major effect of the lean angle.

Nevertheless, it is possible to highlight some limitations of the presented approaches, the main ones being ignoring the ground roughness and slope (in both lateral and forward directions) and neglecting the tires own dynamics (although the overall tire deformability is considered).

The above limitations prevent those models from performing accurate simulations of the dynamics of the motorcycle moving over an effective road surface.

This kind of analysis is crucial for the virtual development of electronic active control systems that are becoming more and more important in motorcycle industry.

In fact, to enhance both safety and performance control systems such as ABS, traction control and stability control (originally developed for four-wheeled vehicles) have been adapted to be installed on road motorcycles.

This process presents a number of issues, and requires a comprehensive virtual vehicle model, capable to accurately describe the higher dynamics of motorcycle tires for a wide frequency range, while ensuring high computational efficiency.

While extensive research efforts have been dedicated to car tires, leading to the development and experimental validation of the so-called rigid-ring tire model (named SWIFT: Short Wavelength Intermediate Frequency Tire Model) [4], only a few papers [5], [6], [7] address to the application of this model to motorcycle tires.

The rigid-ring tire model consists of two rigid bodies, representing the tire belt and the rim respectively. The belt is suspended with all six degrees of freedom (dofs) with respect to the rim, and six spring-damper elements model the sidewall deformability of the tires.

It has been shown [8] that a rigid-ring tire model is able to describe the in-plane (longitudinal and vertical) and out-of-plane (lateral and yaw) tire behaviour up to frequencies of 60 - 100 Hz, where the contribution due to flexible belt modes is negligible.

Aim of this chapter is to develop a comprehensive single-track vehicle model, integrating a rigid-ring tire model, effective road elevation and slope, chain transmission for both driving and braking states and full drivetrain inertia.

To this purpose, a novel approach for the derivation of the equations of motion of a general motorcycle is presented. Starting from the discussion developed in [9], dependent variables are used to determine the front wheel orientation, leading to a simple, computationally fast description of the motorcycle kinematics. This feature makes it possible to easily include rigid-ring tires and road slope without affecting efficiency. The equations of motion are obtained symbolically, using a computer algebra software (CAS), which ensures maximum flexibility and accuracy in the description of the system. The constraint equations due to the dependent coordinates formulation are handled using a projection technique, resulting in an ODE system of equations. This system can be successfully solved not only in the simulation environment presented, but also in real-time applications, such as vehicle state estimation and active vehicle control.

The proposed model will be validated with respect to experimental data in both the time and frequency domains, showing consistent results, accuracy and excellent computational efficiency.

The chapter is organized as follows: the description of the motorcycle geometry and kinematics is followed by the tire and chain transmission models and finally by the derivation of the equations of motion.

1.2 MOTORCYCLE MODEL GEOMETRY

Modern road motorcycles feature a front suspensions of telescopic fork type, rear suspensions of swingarm type (with leverage activating the rear shock absorber), and chain transmissions. The motorcycle model, depicted in Fig. 1.1, consists of eleven rigid bodies: the front and rear tire belts, attached respectively to the front and rear rims (including brake discs), the swingarm (including rear brake caliper and rear suspension strut), the main frame (including rider, engine, rear shock absorber and fuel mass), the front assembly (including fork stanchions, handlebars and steering assembly), the front sprung mass (including lower fork and front brake calipers) and three bodies modelling the rotating inertias of the crankshaft, first gearbox shaft (including clutch) and second gearbox shaft (including drive sprocket).

Although the presented approach makes it possible to easily include the rider movement, it is beyond the scope of this work the discussion of its effect. Hence, the rider is modelled as a mass rigidly attached to the main frame, and the controlling effect due to the rider's body movement is neglected. Vehicle control is due to a steering torque applied on the front assembly and reacting on the main frame (a steering damper is also included), front and rear braking torques, and engine torque. The chain transmission model makes it possible to take into account a braking engine torque as well, since it plays a major role in defining the vehicle's trim during braking maneuvers.

The motorcycle geometry is described by means of three fixed parameters: the swingarm length l_{sa} , the frame length l_r , and the front fork offset l_f . The frame length is defined as the distance between the swingarm pivot and the steering head along the direction orthogonal to the steering axis (frame line), while the front fork offset is the distance between the steering axis and the front wheel axle.

The motorcycle trimming (or internal configuration) can be defined by means of three variables: the angle between swingarm and frame line θ , which depends on the rear suspension extension, the steer angle δ and the front suspension extension f_k .

The motorcycle kinematics are defined in a x-forward, y-right and z-down axis system, which is consistent with SAE conventions. This implies that the roll angle is positive when leaning right as well as steering is positive when heading right; wheel rotations are negative while moving forward.

The positions of the reference frames attached to each body are determined by means of mixed relative coordinates and reference point methods, using the following coordinates and

transformations. The rear wheel axle position and orientation are defined with respect to the ground reference frame. The translations are $\{x,y,z\}$ and the rotations around the x, y and z axes are $\{\varphi,\beta_{y-R},\psi\}$ respectively, being ψ the yaw angle, φ the roll angle and β_{y-R} the road tangent plane forward inclination angle at the rear wheel.

Note that the ground reference frame is the inertial reference system. It is not parallel to the road plane tangent axis system, whose angles are given as a function of the curvilinear abscissa in the inertial reference system.

The swingarm pivot position is defined taking as a reference point the rear wheel axle coordinates. The orientation is given again with respect to the ground, with the rotations $\{\varphi,\mu_2,\psi\}$ being μ_2 the (absolute) swingarm pitch angle. Along the new x-axis a translation of length $\{l_{sa},0,0\}$ leads to the swingarm pivot. The frame head is located similarly taking as a reference point the swingarm pivot position. The rotations are $\{\varphi,\mu_3,\psi\}$ being μ_3 the (absolute) frame pitch angle, and the frame head is reached through a translation of $\{l_r,0,0\}$. Therefore the previously mentioned rear suspension (angular) extension θ can be defined as $\theta = \mu_3 - \mu_2$.

The positions of the upper and lower steering assemblies are given in relative coordinates starting from the frame head. The upper steering reference system is rotated about the previously defined z-axis by the steering angle $\{0,0,\delta\}$ and the lower steering assembly is reached through a translation of length $\{0,0,f_k\}$ along the z-axis. The front wheel axle position is located by means of a further translation of length $\{0,0,l_r\}$ along the x-axis, given by the steering offset.

It is now possible to express the front axle position as a function of the independent variables defined above; the three coordinates, with respect to the rear axle, read:

$$\begin{aligned}
 x_f &= \cos(\delta)\cos(\mu_3)l_f + \cos(\mu_2)l_{sa} + \sin(\mu_3)f_k + \cos(\mu_3)l_r \\
 y_f &= \sin(\varphi)\left[\left(\cos(\delta)l_f + l_r\right)\sin(\mu_3) - \cos(\mu_3)f_k + \sin(\mu_2)l_{sa}\right] + \cos(\varphi)\sin(\delta)l_f \\
 z_f &= \cos(\varphi)\left[-\left(\cos(\delta)l_f + l_r\right)\sin(\mu_3) + \cos(\mu_3)f_k - \sin(\mu_2)l_{sa}\right] + \sin(\varphi)\sin(\delta)l_f
 \end{aligned} \tag{1.1}$$

It is also possible to express the front wheel orientation as a result of the rotations applied to each member of the kinematic chain. Again, starting from the rear axle, the front axle is reached by rolling around the x-axis, then by pitching around the y-axis and finally by

steering around the z-axis. Using the previously introduced angles (and adopting the notation $\cos(\cdot) = c(\cdot)$, $\sin(\cdot) = s(\cdot)$) the overall rotation reads:

$$\mathbf{R}_x(\varphi)\mathbf{R}_y(\mu_3)\mathbf{R}_z(\delta) = \begin{bmatrix} c(\delta)c(\mu_3) & -s(\delta)c(\mu_3) & s(\mu_3) \\ c(\delta)s(\mu_3)s(\varphi) + c(\varphi)s(\delta) & -s(\delta)s(\mu_3)s(\varphi) + c(\varphi)c(\delta) & -c(\mu_3)s(\varphi) \\ -c(\delta)s(\mu_3)c(\varphi) + s(\varphi)s(\delta) & s(\delta)s(\mu_3)c(\varphi) + s(\varphi)c(\delta) & c(\mu_3)c(\varphi) \end{bmatrix} \quad (1.2)$$

where \mathbf{R}_x , \mathbf{R}_y and \mathbf{R}_z are the orthonormal rotation matrices around the three axes.

As it is demonstrated in [9] the front axle orientation can be also obtained by means of three (non-independent) angles, applying the well-known yaw-roll-pitch rotations. Some analytical derivations are given for the sake of clarity. Being φ_f , δ_f , θ_f the roll, yaw and pitch angles of the front axle, the resulting rotation matrix is:

$$\mathbf{R}_z(\delta_f)\mathbf{R}_x(\varphi_f)\mathbf{R}_y(\theta_f) = \begin{bmatrix} c(\delta_f)c(\theta_f) - s(\delta_f)s(\varphi_f)s(\theta_f) & -c(\varphi_f)s(\delta_f) & c(\delta_f)s(\theta_f) + s(\delta_f)s(\varphi_f)c(\theta_f) \\ s(\delta_f)c(\theta_f) + c(\delta_f)s(\varphi_f)s(\theta_f) & c(\varphi_f)c(\delta_f) & s(\delta_f)s(\theta_f) - c(\delta_f)s(\varphi_f)c(\theta_f) \\ -c(\varphi_f)s(\theta_f) & s(\varphi_f) & c(\varphi_f)c(\theta_f) \end{bmatrix} \quad (1.3)$$

Equating (1.2) and (1.3) one obtains:

$$\begin{bmatrix} \varphi_f \\ \theta_f \\ \delta_f \end{bmatrix} = \begin{bmatrix} \sin^{-1}[\sin(\varphi)\cos(\delta) + \cos(\varphi)\sin(\delta)\sin(\mu_3)] \\ \tan^{-1}[(\sin(\mu_3)\cos(\delta) - \tan(\varphi)\sin(\delta)) / \cos(\mu_3)] \\ \tan^{-1}[\cos(\mu_3)\sin(\delta) / (\cos(\varphi)\cos(\delta) - \sin(\varphi)\sin(\delta)\sin(\mu_3))] \end{bmatrix} \quad (1.4)$$

It must be noted that the yaw angle of the front axle δ_f is defined with respect to the motorcycle mid-plane, hence it does not include the overall yaw angle of the motorcycle. This angle is also known as ground steer angle. The yaw angle of the front wheel with respect to the inertial reference frame therefore reads:

$$\psi_f = \delta_f + \psi \quad (1.5)$$

Equation (1.4) makes it possible to express the orientation of the front wheel axle as a function of the orientation of the whole vehicle. Hence the front axle reference frame can be

defined using the reference point method: the coordinates of the reference point are given by Eq. (1.1), the front roll and yaw angles are given by Eqs. (1.4), (1.5) and the pitch angle of the front axle is given by the road tangent plane forward inclination angle β_{y-F} at the front wheel, in short form: $\{\varphi_f, \beta_{y-F}, \psi_f\}$. Therefore the motorcycle kinematics are described by means of 11 independent Lagrangian parameters ($x, y, z, \varphi, \beta_{y-R}, \psi, \mu_2, \mu_3, \delta, f_k, \beta_{y-F}$) and 2 dependent coordinates (φ_f, ψ_f). This choice makes it possible to avoid the extremely involved expression resulting from a full independent-coordinates description, thus reducing the dimension of the model and the computational effort, but requires to handle two algebraic constraint equations during the numerical integration of the equations of motion. The kinematics of the rigid-ring model and of the chain transmission will be analyzed in the following sections.

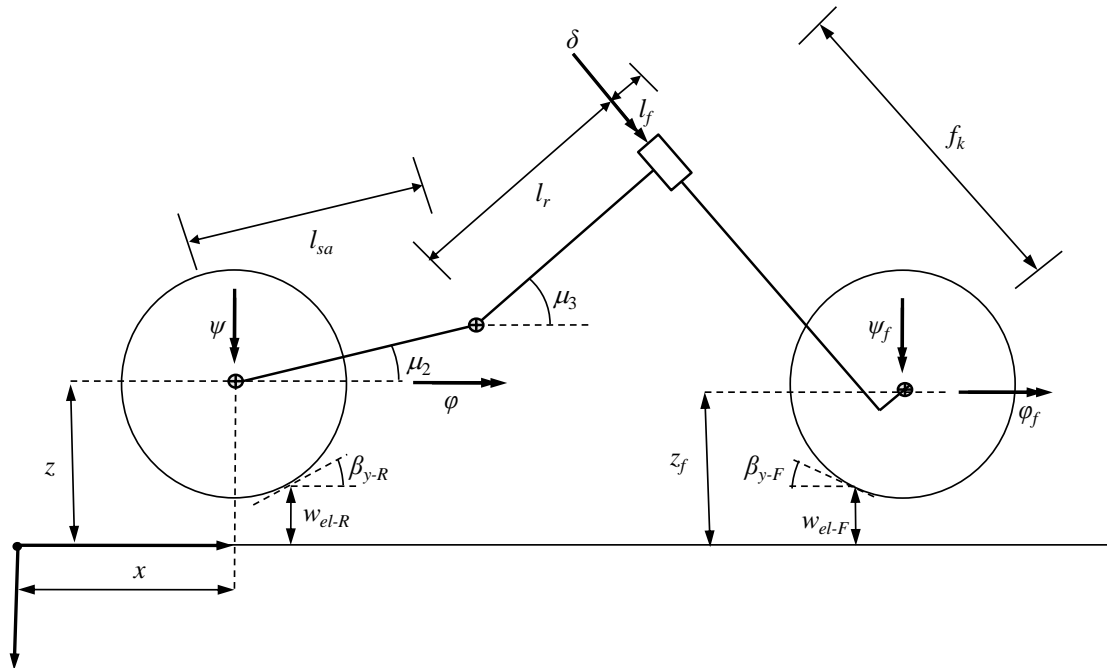


Fig. 1.1: Schematic of the motorcycle model.

1.3 RIGID RING TIRE MODEL

The rigid-ring tire model (Fig. 1.2) consists of two rigid bodies. The first (from now on called the rim) includes the inertial properties of the rim and the inner part of the tire sidewall moving together with the rim, while the second (from now on called the belt) takes into account the inertial properties of the remaining parts of the tire [10]. The rim is attached to the wheel axle reference frame, while the belt is suspended with respect to the rim with six dofs as already stated.

The following analysis holds for both the front and rear tires: their axle positions and orientations are given by $\{x, y, z\}$, $\{\varphi, \beta_{y-R}, \psi\}$ for the rear wheel and by $\{x_f, y_f, z_f\}$, $\{\varphi_f, \beta_{y-F}, \psi_f\}$ for the front wheel. The subscript a from now on will identify the rim reference frame, while the subscript rb will identify the belt reference system, either for front and rear wheel.

The kinematics of the rigid-ring model are derived using relative coordinates starting from the wheel axle non-rotating reference frame. The rotating reference frame is easily obtained by pre-multiplication of the rotation matrix $\mathbf{R}_y(\theta_a)$.

The position of the center of the belt is reached with three translations (x_{rb} , y_{rb} , z_{rb}) from the center of the rim and three further positive rotations (namely ψ_{rb} , φ_{rb} , θ_{rb}), define its orientation. Since the deformations of the tire sidewalls are small, the rotation matrices can be linearized and higher order terms neglected. Applying the usual yaw-roll-pitch series of rotations, a vector \mathbf{v} given in the belt reference frame (subscript rb) can be expressed in the rim reference frame (subscript a) by applying the rotation matrix R_{rb-a} [11]:

$$\mathbf{v}_a = \mathbf{R}_{rb-a} \mathbf{v}_{rb}, \quad \mathbf{R}_{rb-a} = \mathbf{R}_z(-\psi_{rb}) \mathbf{R}_x(-\varphi_{rb}) \mathbf{R}_y(-\theta_{rb}) = \begin{bmatrix} 1 & -\psi_{rb} & \theta_{rb} \\ \psi_{rb} & 1 & -\varphi_{rb} \\ -\theta_{rb} & \varphi_{rb} & 1 \end{bmatrix} \quad (1.6)$$

The forces between the rim and the belt are due to six linear spring-damper systems. While the forces due to the springs are defined in the non-rotating reference system, dampers are rotating along with the wheel. This leads to coupling terms in the damping forces. The components of the absolute angular velocity $\mathbf{\Omega}$ of the rim (given in the rim non-rotating reference frame) are:

$$\mathbf{\Omega}_a = \begin{bmatrix} \dot{\varphi}_a \\ \omega_a + \dot{\psi}_a \sin(\varphi_a) \\ \dot{\psi}_a \cos(\varphi_a) \end{bmatrix} \quad (1.7)$$

where $\dot{\psi}_a$ is the yaw angular velocity (in the ground reference frame), $\dot{\varphi}_a$ is the roll angular velocity (in the rim reference frame) and ω_a is the rotating speed of the rim, leading to the following expression for the forces and moments of the springs and dampers in the non-rotating frame [11]:

$$\begin{aligned} F_{xrb} &= k_x x_{rb} + c_x \dot{x}_{rb} - c_z z_{rb} [\omega_a + \dot{\psi}_a \sin(\varphi_a)] \\ F_{yrb} &= k_y y_{rb} + c_y \dot{y}_{rb} \\ F_{zrb} &= k_z z_{rb} + c_z \dot{z}_{rb} + c_x x_{rb} [\omega_a + \dot{\psi}_a \sin(\varphi_a)] \\ M_{xrb} &= k_\varphi \varphi_{rb} + c_\varphi \dot{\varphi}_{rb} - c_\psi \psi_{rb} [\omega_a + \dot{\psi}_a \sin(\varphi_a)] \\ M_{yrb} &= k_\theta \theta_{rb} + c_\theta \dot{\theta}_{rb} \\ M_{zrb} &= k_\psi \psi_{rb} + c_\psi \dot{\psi}_{rb} + c_\varphi \varphi_{rb} [\omega_a + \dot{\psi}_a \sin(\varphi_a)] \end{aligned} \quad (1.8)$$

in which second order terms were neglected (due to the small values of x_{rb} , y_{rb} , z_{rb} and ψ_{rb} , φ_{rb} , θ_{rb}).

In order to properly model the tire overall lateral and radial stiffness, two spring-damper systems are added in series with those of the rigid-ring model, between the belt and the ground contact point. In fact, the rigid-ring stiffness are chosen in order to simulate the high frequency behaviour of the tire, while not ensuring the effective overall deformability. Moreover, it is well known that the overall tire stiffness is nonlinear, depending on vertical load and forward velocity, so that the residual stiffness must respect this relation:

$$\begin{aligned} \frac{1}{k_{rad}} &= \frac{1}{k_{rr}} + \frac{1}{k_x} \\ \frac{1}{k_{lat}} &= \frac{1}{k_{lr}} + \frac{1}{k_y} \end{aligned} \quad (1.9)$$

where k_{rad} and k_{lat} are the overall lateral and radial stiffness of the tire and k_{rr} , k_{lr} are the residual radial and lateral stiffness.

The profile of the tire is assumed to be torus-shaped, so that, starting from the belt center, the contact point is reached through the following translation of coordinates:

$$\begin{aligned}
 x_{cp} &= 0 \\
 y_{cp} &= \rho \sin(\varphi - \beta_x) - y_{lat} \\
 z_{cp} &= r - \rho \cdot [1 - \cos(\varphi - \beta_x)] - z_{rad}
 \end{aligned}
 \tag{1.10}$$

where ρ is the radius of the torus, r is the maximum radius of the tire, β_x is the angle of lateral slope (with respect to the inertial reference frame) of the plane tangent to the road surface in the contact point and y_{lat} , z_{rad} are the lateral and radial residual deformations.

A contact mass with translational inertia is added at the ground contact point [6]. Acting on the contact mass are the forces of residual springs and damper (in tilted direction), the tire-ground normal contact force, and the tire driving forces. The forces of the residual springs and dampers read:

$$\begin{aligned}
 F_{rad} &= k_{rr} z_{rad} + c_{rr} \dot{z}_{rad} \\
 F_{lat} &= k_{lr} y_{lat} + c_{lr} \dot{y}_{lat}
 \end{aligned}
 \tag{1.11}$$

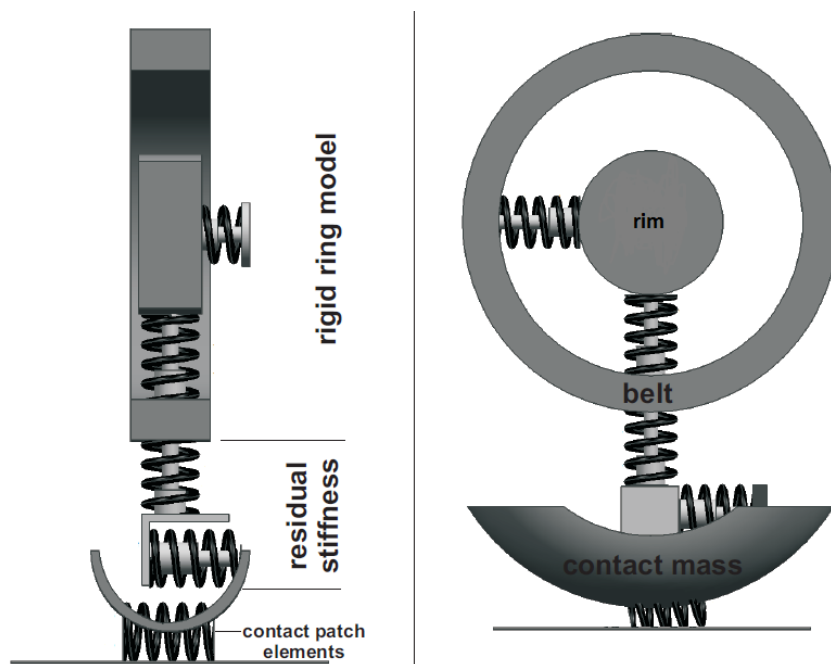


Fig. 1.2: Schematic of the rigid-ring tire model.

The tire-ground normal force is calculated considering the ground contact as a deformable unilateral holonomous constraint. The normal force in the ground reference system hence is:

$$F_N = k_{gr} \cdot z_{eff} \cdot \cos(\beta_x) \cos(\beta_y) \quad \begin{cases} z_{eff} = w_{el} - z_{cp} & \text{if } z_{cp} \leq w_{el} \\ z_{eff} = 0 & \text{if } z_{cp} > w_{el} \end{cases} \quad (1.12)$$

where k_{gr} is the ground stiffness, w_{el} is the effective road elevation and z_{cp} is the elevation of the contact mass, both elevations with respect to the inertial reference system.

The tire driving forces are described using the well-known empirical ‘‘Magic Formulas’’ (MF) for motorcycle tires, as described in [12]. Input quantities for the MF are: the vertical load F_N , the wheel camber angle (which equals $\varphi - \beta_x$), the longitudinal and lateral slip factors. The driving forces are applied to the contact mass, so no overturning moment is considered. Rolling resistance and self-aligning torque are applied to the belt.

In order to properly calculate the slip factors it is necessary to define the slip velocities of the contact mass. The longitudinal and lateral slip, κ and α , in stationary conditions are defined as:

$$\begin{aligned} \kappa &= -\frac{VSX}{VX} \\ \tan(\alpha) &= \frac{VSY}{VX} \end{aligned} \quad (1.13)$$

where VX , VSX and VSY are velocities which can be calculated by means of the transformation T_{0-a} , that defines the position of a point given in the inertial reference system O in the rim reference system a , applied to the position of the contact point P :

$$\begin{aligned} P_a &= T_{0-a} \cdot P_0 \\ v_P &= T_{0-a} \cdot \dot{P}_0 + \dot{T}_{0-a} \cdot P_0 \end{aligned} \quad (1.14)$$

The absolute velocity v of the contact point is composed of two terms: the first is the relative velocity of the contact point with respect to the rim and the second term is the velocity of a point instantaneously coincident with the contact point and belonging to the rim rotating

reference system, also known as eulerian velocity of the contact point. The speed VX is the x-component of v_p and VSX , VSY are the x and y-components of the so-called eulerian velocity. When an experimental estimate of the actual rolling radius R_e of the tire as account this dependence by defining the longitudinal slip factor as [4]:

$$\kappa = -1 + \frac{\omega_a \cdot R_e}{VX} \quad (1.15)$$

The actual expressions are not shown due to their large size, but it must be noted that both lateral and longitudinal slips depend on rigid-ring deformations, residual deformations and road slopes.

In order to model the tire-thread own dynamics the above defined slip is not directly fed to the Magic Formula. A relaxation model is introduced instead, which makes it possible to describe the contact patch deformation by introducing a time delay defined by a relaxation length. The relaxation equations are defined below, being u and v the contact patch deformations in longitudinal and lateral direction:

$$\begin{aligned} \sigma_k \frac{du}{dt} + VX \cdot u &= -\sigma_k \cdot VSX \\ \sigma_\alpha \frac{dv}{dt} + VX \cdot v &= -\sigma_\alpha \cdot VSY \end{aligned} \quad (1.16)$$

From Eq. (1.16) it is possible to calculate the actual slip factors using the relations:

$$\begin{aligned} \kappa &= \frac{u}{\sigma_k} \\ \tan(\alpha) &= \frac{v}{\sigma_\alpha} \end{aligned} \quad (1.17)$$

The relaxation lengths are not constant, since they depend on the tire overall (longitudinal and lateral) stiffness C and on the slip and cornering stiffness K , that, in turn, depend on the vertical load:

$$\sigma_\kappa = \frac{K_{x\kappa}}{C_x}$$

$$\sigma_\alpha = \frac{K_{y\alpha}}{C_y}$$
(1.18)

1.4 TRANSMISSION MODEL

The adopted transmission model features three (rigid) bodies with rotational inertias modelling the crankshaft and the gearbox. The angular velocity of the gearbox output shaft θ_{ds} is the only independent variable, while the angular velocities of the remaining shafts are determined by the actual gear ratio and the primary reduction gear ratio. The engine torque is applied to the crankshaft. Transmission efficiency is also included.

The chain is modelled as a massless visco-elastic thread wrapped around the pinion (radius r_{ds}) and the chainwheel (radius r_{ws}). When the upper (lower) segment of the chain is stretched, it becomes tangent to both the pinion and the chainwheel, in the points A, C (B, D) as shown in Fig. 1.3:

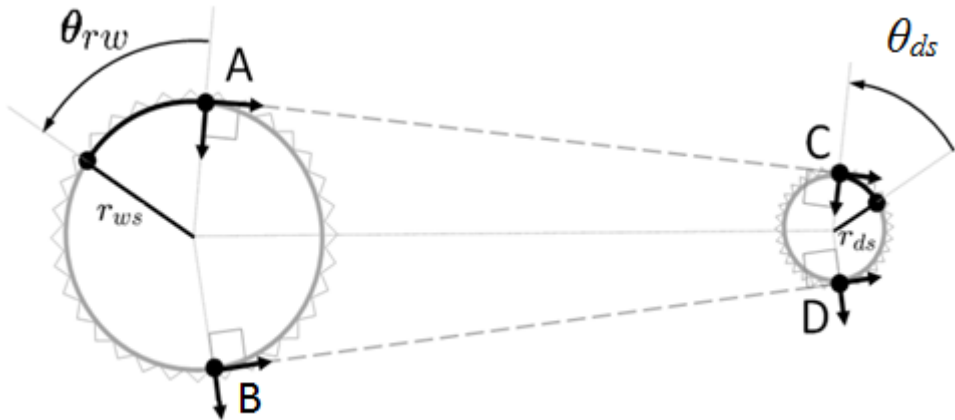


Fig. 1.3: Chain transmission model.

It is possible to locate the tangent points by means of the following geometric quantities:

$$\begin{aligned}
 \theta &= \mu_2 - \mu_3 \\
 \cos(\alpha) &= (r_{ws} - r_{ds})/d_{ia} \\
 \tan(\beta) &= [x_{ds} \cdot \sin(\theta) + z_{ds} \cdot \cos(\theta)]/d_{ia} \\
 d_{ia} &= l_{sa} + x_{ds} \cdot \cos(\theta) - z_{ds} \cdot \sin(\theta)
 \end{aligned}
 \tag{1.19}$$

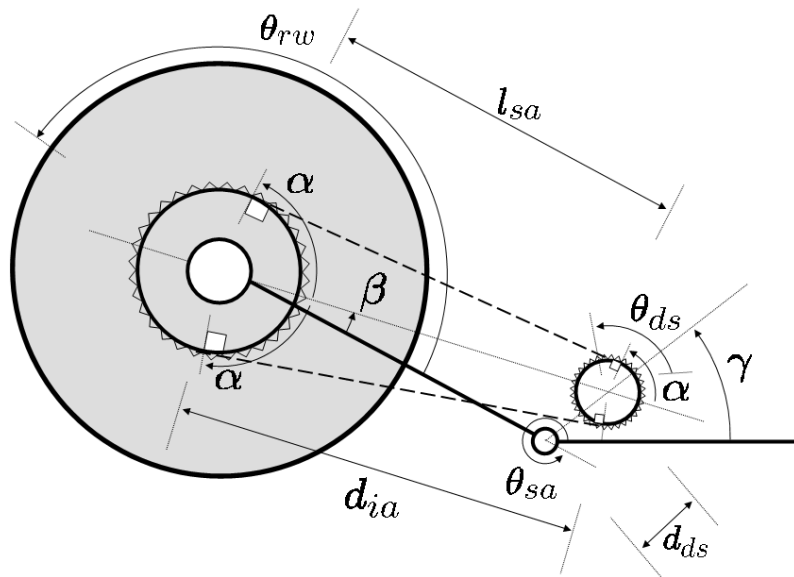


Fig. 1.4: Chain transmission kinematics.

In points A, C (B, D) a force is applied as depicted in Fig. 1.5, acting on both pinion and chainwheel along the chain line and in opposite direction. This force is proportional to the chain extension and to the relative speed between tangent points A, C (B, D), according to:

$$\begin{aligned}
 T_u &= \begin{cases} k \cdot e_u + c \cdot \frac{de_u}{dt} & \text{if } e_u \geq 0 \\ 0 & \text{if } e_u < 0 \end{cases} \\
 T_l &= \begin{cases} k \cdot e_l + c \cdot \frac{de_l}{dt} & \text{if } e_l \geq 0 \\ 0 & \text{if } e_l < 0 \end{cases}
 \end{aligned}
 \tag{1.20}$$

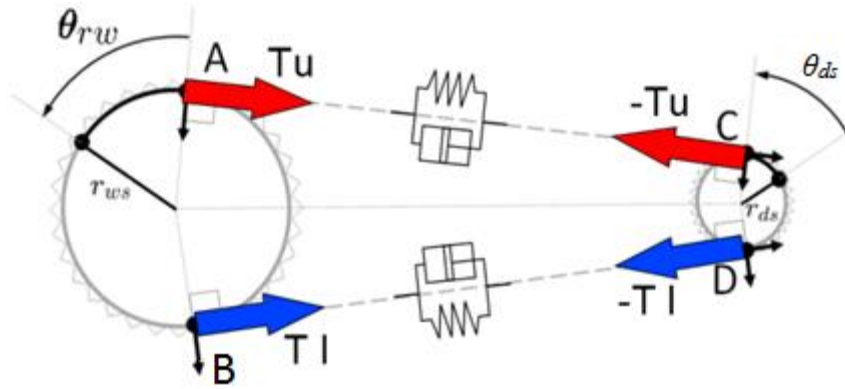


Fig. 1.5: Chain transmission forces.

where the chain extension e_u (e_l) is defined as the difference between the upper (lower) rest length (which is a parameter of the model) and the upper (lower) length. The upper (lower) length depends on the pinion and chainwheel angular displacements θ_{ds} and θ_{wr} , as well as on the unstretched chain length l_u^0 (l_l^0):

$$\begin{aligned} \overline{AC} = \overline{BD} &= \sqrt{d_{ia}^2 + (r_{ws} - r_{ds})^2} \\ e_u &= r_{ws} \cdot \theta_{wr}(t) + \overline{AC} - r_{ds} \cdot \theta_{ds}(t) - l_u^0 \\ e_l &= -r_{ws} \cdot \theta_{wr}(t) + \overline{BD} + r_{ds} \cdot \theta_{ds}(t) - l_l^0 \end{aligned} \quad (1.21)$$

If the sum of the upper and lower unstretched chain lengths is large enough, the two segments are never in tension at the same time.

An upper limit is imposed to the maximum engine braking torque, in order to model the anti-hop clutch effect featured in modern four-stroke racing motorcycles.

1.5 DERIVATION OF THE EQUATIONS OF MOTION

The equations of motion are automatically generated using a symbolic formalism within a MAPLE software environment. A set of symbolic multibody procedures developed by Lot [13] is adopted to define the reference systems attached to each body as well as the applied forces and torques. The equations of motion can be obtained through a Lagrange [14] or a Newton-Euler [15] approach, the latter being most suitable in the case of a linearized system. Using the full set of redundant coordinates, both techniques result in a second order ODE system in the following form, where \mathbf{M} denotes a mass matrix (time dependent, positively defined) and \mathbf{f} denotes the vector of applied forces and terms dependent on displacements and velocities:

$$\mathbf{M}(\mathbf{q}) \cdot \ddot{\mathbf{q}} = \mathbf{f}(\mathbf{q}, \dot{\mathbf{q}}, t) \quad (1.22)$$

Equation (1.22) can also be written using the well-known state-space transformation as follows:

$$\frac{d}{dt} \begin{bmatrix} \mathbf{q}(t) \\ \dot{\mathbf{q}}(t) \end{bmatrix} = \begin{bmatrix} \dot{\mathbf{q}}(t) \\ \mathbf{M}^{-1}(\mathbf{q}, t) \cdot \mathbf{f}(\dot{\mathbf{q}}, \mathbf{q}, t) \end{bmatrix} \quad (1.23)$$

Since not all the coordinates are independent, a system of holonomous constraint equations \mathbf{g} (with Jacobian matrix Φ) must be satisfied:

$$\mathbf{g}(\mathbf{q}, t) = 0, \quad \Phi(\mathbf{q}, t) = \frac{\partial \mathbf{g}(\mathbf{q}, t)}{\partial \mathbf{q}} \quad (1.24)$$

Introducing the Lagrange multipliers $\lambda(t)$ and the constraint equations (1.24), the system Eq. (1.22) becomes an index-3 DAE system:

$$\mathbf{M}(\mathbf{q}) \cdot \ddot{\mathbf{q}} = \mathbf{f}(\mathbf{q}, \dot{\mathbf{q}}, t) - \Phi(\mathbf{q}, t) \cdot \lambda(t) \quad (1.25)$$

The dimension of \mathbf{g} (and therefore of λ) depends on the selected approach for modelling the system kinematics. Using natural coordinates, for example, leads to as many constraint equations as many joints in the system. This approach was adopted in [1], leading to a large number of constraint equations (although very simple) to be satisfied during numerical integration, for which the Baumgarte stabilization method was successfully applied.

The kinematic constraints Eq. (1.24) imposed at the displacement level, must hold at the velocity and acceleration levels as well [16]. By derivation w.r.t. time one obtains:

$$\begin{aligned} \frac{d}{dt} \mathbf{g}(\mathbf{q}, t) &= \frac{\partial}{\partial t} \mathbf{g}(\mathbf{q}, t) + \frac{\partial}{\partial \mathbf{q}} \mathbf{g}(\mathbf{q}, t) \cdot \frac{d\mathbf{q}}{dt} = \frac{\partial}{\partial t} \mathbf{g}(\mathbf{q}, t) + \Phi(\mathbf{q}, t) \cdot \dot{\mathbf{q}} = 0 \\ \frac{d^2}{dt^2} \mathbf{g}(\mathbf{q}, t) &= \frac{\partial^2}{\partial t^2} \mathbf{g}(\mathbf{q}, t) + \frac{\partial}{\partial \mathbf{q}} \mathbf{g}(\mathbf{q}, t) \cdot \frac{d^2 \mathbf{q}}{dt^2} + \frac{d}{dt} \left(\frac{\partial}{\partial \mathbf{q}} \mathbf{g}(\mathbf{q}, t) \right) \cdot \frac{d\mathbf{q}}{dt} = \\ &= \frac{\partial^2}{\partial t^2} \mathbf{g}(\mathbf{q}, t) + \Phi(\mathbf{q}, t) \cdot \ddot{\mathbf{q}} + \frac{d}{dt} \Phi(\mathbf{q}, t) \cdot \dot{\mathbf{q}} = 0 \end{aligned} \quad (1.26)$$

and, consequently:

$$\begin{aligned} \frac{\partial}{\partial t} \mathbf{g}(\mathbf{q}, t) &= -\Phi(\mathbf{q}, t) \cdot \dot{\mathbf{q}} \\ \frac{\partial^2}{\partial t^2} \mathbf{g}(\mathbf{q}, t) &= -\Phi(\mathbf{q}, t) \cdot \ddot{\mathbf{q}} - \dot{\Phi}(\mathbf{q}, t) \cdot \dot{\mathbf{q}} \end{aligned} \quad (1.27)$$

The simultaneous solution of Eq. (1.25) as long as conditions (1.26) leads to the system:

$$\begin{bmatrix} \mathbf{M}(\mathbf{q}, t) & \Phi^T(\mathbf{q}, t) \\ \Phi(\mathbf{q}, t) & \mathbf{0} \end{bmatrix} \cdot \begin{bmatrix} \ddot{\mathbf{q}}(t) \\ \lambda(\mathbf{q}, t) \end{bmatrix} = \begin{bmatrix} \mathbf{f}(\mathbf{q}, \dot{\mathbf{q}}, t) \\ -\frac{\partial^2}{\partial t^2} \mathbf{g}(\mathbf{q}, t) - \dot{\Phi}(\mathbf{q}, t) \cdot \dot{\mathbf{q}} \end{bmatrix} \quad (1.28)$$

The system Eq. (1.28) has n unknowns, being n the dimension of the full set of dependent coordinates, and it has m Lagrange multipliers. That is, the system has $f = n - m$ independent coordinates (dofs).

In the case of scleronomous constraints (constraint equations not explicitly time dependent) it is possible to partition the dependent coordinates q_d from the independent ones q_i . Then the first of Eqs. (1.27) becomes:

$$\mathbf{0} = [\Phi_d \quad \Phi_i] \cdot \begin{bmatrix} \dot{\mathbf{q}}_d \\ \dot{\mathbf{q}}_i \equiv \dot{\mathbf{z}} \end{bmatrix} \quad (1.29)$$

If matrix Φ_d is invertible, it is possible to express the dependent velocities as a function of the independent ones as:

$$\dot{\mathbf{q}}_d = -(\Phi_d)^{-1} \cdot \Phi_i \dot{\mathbf{z}} \quad (1.30)$$

establishing the following relation between the velocities:

$$\dot{\mathbf{q}} = \mathbf{R} \cdot \dot{\mathbf{z}}, \quad \mathbf{R} = \begin{bmatrix} -(\Phi_d)^{-1} \cdot \Phi_i \\ \mathbf{I} \end{bmatrix} \quad (1.31)$$

Since matrix Φ_d is invertible it has full rank, that is m independent columns, and n rows. Its nullspace represents the subspace of allowable motions of the system: hence the velocity of any point (compatible with constraints) must belong to this subspace [17].

By differentiating w.r.t. time Eq. (1.31) the projection operator for accelerations is obtained:

$$\ddot{\mathbf{q}} = \dot{\mathbf{R}}\dot{\mathbf{z}} + \mathbf{R}\ddot{\mathbf{z}} \quad (1.32)$$

By partitioning the acceleration vector the constraint equation Eq. (1.27) becomes:

$$[\Phi_d \quad \Phi_i] \begin{Bmatrix} \ddot{\mathbf{q}}_d \\ \ddot{\mathbf{z}} \end{Bmatrix} = -[\dot{\Phi}_d \quad \dot{\Phi}_i] \begin{Bmatrix} \dot{\mathbf{q}}_d \\ \dot{\mathbf{z}} \end{Bmatrix} \quad (1.33)$$

In order to obtain the term $\dot{\mathbf{R}}\dot{\mathbf{z}}$, note that it represents the system accelerations in the case of null independent accelerations. From Eq. (1.33) for $\ddot{\mathbf{z}} = 0$ one obtains:

$$\dot{\mathbf{R}}\dot{\mathbf{z}} \Big|_{\ddot{\mathbf{z}}=0} = \begin{Bmatrix} \ddot{\mathbf{q}}_d \\ \ddot{\mathbf{z}} \end{Bmatrix}_{\ddot{\mathbf{z}}=0} = \begin{Bmatrix} -(\Phi_d)^T \dot{\Phi}_d \dot{\mathbf{q}}_d \\ \mathbf{0} \end{Bmatrix} \quad (1.34)$$

Substituting $\ddot{\mathbf{q}}$ in the first row of Eq. (1.28) and pre-multiplying by \mathbf{R}^T it is possible to obtain the equations of motion in independent coordinates as:

$$\mathbf{R}^T(\mathbf{z}) \cdot \mathbf{M}(\mathbf{z}) \cdot \mathbf{R}(\mathbf{z}) \cdot \ddot{\mathbf{z}}(t) = \mathbf{R}^T(\mathbf{z}) \cdot \mathbf{f}(\dot{\mathbf{z}}, \mathbf{z}) - \mathbf{R}^T(\mathbf{z}) \cdot \mathbf{M}(\mathbf{z}) \cdot \dot{\mathbf{R}}(\mathbf{z}) \cdot \dot{\mathbf{z}}(t) \quad (1.35)$$

The independent coordinates formulation in Eq. (1.35) is only valid locally (where the parametrization is well-defined). It requires the construction of matrix \mathbf{R} , and the evaluation of the dependent displacements and velocities at each integration step, even if only the independent coordinates are integrated. In conventional formulations it is necessary to check the linear independence of the chosen parametrization at each function evaluation, using the properties of Jacobian matrix. Frequent reparametrizations hence may be required as well as the numerical evaluation of large coefficients matrices in Eq. (1.35), which can affect computational efficiency, especially in case of multistep solvers [18]. In the presented approach an optimal parametrization is adopted, which is well-defined for all feasible motorcycle motions (namely when both the roll and steering angle are in the range of $\pm 90^\circ$) and therefore does not require checking or modifications during the integration. Moreover Eq. (1.35) is implemented symbolically, so the coefficients are prepared before the simulation in order to make their evaluation efficient. Finally, due to the adopted parametrization, it is possible to obtain uncoupled constraint equations, so that dependent displacements and velocities are computed at each time step without any further matrix inversion.

It has been shown in Eq. (1.4) how to relate the dependent orientation coordinates for the front wheel (φ_f, δ_f) to the independent (Lagrangian) parameters describing the vehicle kinematics. In ref. [9] a detailed analysis of the domain of definition for those equations is given, showing that equations are not only consistently defined but also are continuously differentiable on $[-\pi/2, \pi/2]$. It is hence possible to state a set of constraint equations by rearranging Eq. (1.4) as:

$$\begin{cases} s(\delta_f)[c(\varphi) \cdot c(\delta) - s(\varphi) \cdot s(\mu_3) \cdot s(\delta)] = c(\delta_f) \cdot c(\mu_3) \cdot s(\delta) \\ s(\varphi_f) = c(\varphi) \cdot s(\mu_3) \cdot s(\delta) + s(\varphi) \cdot c(\delta) \end{cases} \quad (1.36)$$

By computing the time derivative of Eq. (1.36) it is possible to express the constraints at the velocity level. Moreover, is possible to calculate the matrices Φ_d and Φ_i by collecting the terms multiplying the dependent and independent velocities, respectively. The following expression for the matrix Φ_d is obtained:

$$\Phi_d = \begin{bmatrix} c(\delta_f)[s(\mu_3)s(\varphi)s(\delta) - c(\varphi)c(\delta)] - s(\delta_f)c(\mu_3)s(\delta) & 0 \\ 0 & c(\varphi_f) \end{bmatrix} \quad (1.37)$$

Being Eqs. (1.36) uncoupled, the resulting Jacobian sub-matrix is diagonal, has full rank within the domain, and the calculation of the inverse matrix required in Eq. (1.30) is trivial.

The matrix Φ_i is shown next, considering only the terms involved by the constraints:

$$\Phi_i^T = \begin{bmatrix} s(\delta_f)[c(\varphi)s(\mu_3)s(\delta) + c(\delta)s(\varphi)] & s(\varphi)s(\mu_3)s(\delta) - c(\delta)c(\varphi) \\ s(\delta_f)[s(\mu_3)s(\varphi)c(\delta) + c(\varphi)s(\delta)] + c(\delta_f)c(\mu_3)c(\delta) & s(\delta)s(\varphi) - s(\mu_3)c(\varphi)c(\delta) \\ s(\delta_f)c(\mu_3)s(\varphi)s(\delta) - c(\delta_f)s(\mu_3)s(\delta) & -c(\mu_3)c(\varphi)s(\delta) \end{bmatrix} \quad (1.38)$$

It is now possible to assemble matrix \mathbf{R} using Eq. (1.31), obtaining (for the terms involved):

$$\mathbf{R}^T = - \begin{bmatrix} \frac{s(\delta_f)[c(\varphi)s(\mu_3)s(\delta) + c(\delta)s(\varphi)]}{c(\delta_f)[s(\mu_3)s(\varphi)s(\delta) - c(\varphi)c(\delta)] - s(\delta_f)c(\mu_3)s(\delta)} & \frac{s(\varphi)s(\mu_3)s(\delta) - c(\delta)c(\varphi)}{c(\varphi_f)} \\ \frac{s(\delta_f)[s(\mu_3)s(\varphi)c(\delta) + c(\varphi)s(\delta)] + c(\delta_f)c(\mu_3)c(\delta)}{c(\delta_f)[s(\mu_3)s(\varphi)s(\delta) - c(\varphi)c(\delta)] - s(\delta_f)c(\mu_3)s(\delta)} & \frac{s(\delta)s(\varphi) - s(\mu_3)c(\varphi)c(\delta)}{c(\varphi_f)} \\ \frac{s(\delta_f)c(\mu_3)s(\varphi)s(\delta) - c(\delta_f)s(\mu_3)s(\delta)}{c(\delta_f)[s(\mu_3)s(\varphi)s(\delta) - c(\varphi)c(\delta)] - s(\delta_f)c(\mu_3)s(\delta)} & \frac{-c(\mu_3)c(\varphi)s(\delta)}{c(\varphi_f)} \end{bmatrix} \quad (1.39)$$

At this stage the computation of vector $\dot{\mathbf{R}}\dot{\mathbf{z}}$ is straightforward by means of derivation w.r.t. time. All the operations from Eq. (1.29) to Eq. (1.35) have been implemented in a MAPLE procedure, where the equations of motion of the unconstrained system are computed as well, using the library presented in [13]. Finally, the equations of motions have been reformulated symbolically in terms of independent coordinates as shown in Eq. (1.35), and only independent coordinates are integrated. The solving algorithm therefore is:

- 1) The state vector $\mathbf{y} = \{\dot{\mathbf{z}}, \mathbf{z}\}$ is received from the integrator. Using Eqs. (1.4) and (1.31) the dependent displacement and velocities are obtained. This operation is computationally inexpensive due to uncoupled constraint equations.
- 2) The independent accelerations are immediately computed using Eq. (1.35). Note that all of the matrices are pre-computed symbolically and no check on the parametrization is needed. The only computational efforts are matrix evaluation and numerical inversion.
- 3) The state vector $\ddot{\mathbf{y}} = \{\ddot{\mathbf{z}}, \dot{\mathbf{z}}\}$ is assembled and returned to the integrator.

The numerical integration was performed using an algorithm based on backward differentiation formulae (BDFs) available in Matlab environment (ODE15s), one of the most often used time-integration methods for stiff technical systems, due to its higher order of convergence compared to backward Euler method [16] and adaptive computation stepsize. The large number of function evaluations required to numerically compute the Jacobian matrix during integration does not affect the overall computational efficiency due to the efficient approach adopted in the derivation of the equations of motion. However note that the adopted symbolic approach makes it possible to easily obtain the expression of the Jacobian matrix in symbolic form, which can be directly passed to the integrator, avoiding the above mentioned numerical evaluation and thus further improving computation times.

1.6 MODEL SUMMARY

Finally a summary of the model features is given, in order to provide a comprehensive view of its architecture.

Independent coordinates (rotations are not linearized where not explicitly stated):

- x, y, z , translational displacements of the rear wheel axle center w.r.t. to the inertial reference system,
- φ, ψ : roll and yaw angles of the rear wheel axle w.r.t. to the inertial reference system,
- μ_2, μ_3 : pitch angles of the swingarm and frame w.r.t. to the inertial reference system,
- δ : steering angle,
- fk : translational displacement of the front suspension,
- θ_{ds} : rotation angle of the drive sprocket w.r.t. to the inertial reference system,
- θ_{Fw}, θ_{Rw} : rotation angle of the wheels w.r.t. to the inertial reference system,
- $x_{rb-F}, y_{rb-F}, z_{rb-F}$: translational displacements of the front tire belt, w.r.t. front wheel axle,
- $\varphi_{rb-F}, \theta_{rb-F}, \psi_{rb-F}$: linearized angular displacements of the front tire belt w.r.t. front wheel axle,
- z_{rad-F}, y_{lat-F} : radial and lateral residual front displacements, w.r.t. front tire belt,
- $x_{rb-R}, y_{rb-R}, z_{rb-R}$: translational displacement of the rear tire belt, w.r.t. rear wheel axle,
- $\varphi_{rb-R}, \theta_{rb-R}, \psi_{rb-R}$: linearized angular displacements of the rear tire belt w.r.t. rear wheel axle,
- z_{rad-R}, y_{lat-R} : radial and lateral residual rear displacements, w.r.t. rear tire belt,
- u_f, u_r : front and rear contact patch longitudinal deformations,
- v_f, v_r : front and rear contact patch lateral deformations.

Dependent coordinates

- φ_f, ψ_f : roll and yaw angles of the front wheel axle w.r.t. to the inertial reference system.

Kinematic input quantities

- $\beta_{x-F}, \beta_{y-F}, w_{el-F}$: lateral and longitudinal road surface slopes and road elevation at the front contact point w.r.t. to the inertial reference system,
- $\beta_{x-R}, \beta_{y-R}, w_{el-R}$: lateral and longitudinal road surface slopes and road elevation at the rear contact point w.r.t. to the inertial reference system.

The resulting state vector therefore has $32 \times 2 = 64$ components, since the dependent coordinates are not integrated, and road elevation and slopes are taken into account as input parameters.

Each rigid body constituting the multibody model is associated with a mass and a tensor of inertia.

Rigid bodies

- front and rear contact masses,
- front and rear tire belts,
- front and rear rims,
- swingarm and mainframe (including engine and rider),
- upper and lower steering assemblies,
- crankshaft, gearbox first and second shafts.

Controls

- M_{st} : steering torque, acting on the upper steering assembly (reacting on the frame),
- M_e : engine torque, acting on the crankshaft,
- M_{b-F} : front brake torque, acting on the front rim (reacting on the lower steering assembly),
- M_{b-R} : rear brake torque, acting on the rear rim (reacting on the swingarm).

The applied forces and torques can be classified as external and internal. The external forces and torques are due to aerodynamic actions and tire-ground forces. The aerodynamic actions are modelled as three forces applied at ground level in the wheelbase midpoint and three torques. The aerodynamic coefficients were determined by means of wind tunnel testing, for both a prone rider and a standing rider, and for both leaning and straight running configurations. Using the actual roll angle and applied brake and engine torques it is possible to properly chose the set of aerodynamic coefficients during numerical simulations. The tire forces are modelled using Magic Formulas as stated in section 1.3.

The internal forces are due to spring-damper systems. While the rigid-ring spring-damper systems are fully linear, the residual spring-damper systems feature non-linear stiffness. The front suspension, which is not activated by a leverage, has a tri-linear elastic characteristic (modelling the spring, the bottom out bumper and the top out spring) and a non-linear damping characteristic, which will be described in detail in chapter 2. The rear suspension,

while sharing with the front one the shock absorber model, is activated by a leverage, which converts the angular relative motion of the swingarm with respect to the frame into a translational compression of the shock absorber. In order to obtain the equivalent rotational spring-damper system, the procedure presented in [3] was applied. The steering damper is modelled as purely linear, acting on the upper steering assembly (reacting on the frame). The last internal force is the chain force which acts on chainwheel and sprocket.

Internal forces and torques

- M_{st-D} : steering damper torque (linear),
- M_{sh} : rear suspension visco-elastic torque (non-linear),
- F_{fk} : front suspension visco-elastic force (non-linear),
- $F_{x-rb-F}, F_{y-rb-F}, F_{z-rb-F}, M_{x-rb-F}, M_{y-rb-F}, M_{z-rb-F}$: front rigid ring forces and torques (linear),
- F_{rad-F}, F_{lat-F} : front tire residual forces (non-linear),
- $F_{x-rb-R}, F_{y-rb-R}, F_{z-rb-R}, M_{x-rb-R}, M_{y-rb-R}, M_{z-rb-R}$: rear rigid ring forces and torques (linear),
- F_{rad-R}, F_{lat-R} : rear tire residual forces (non-linear),
- F_{ch-L}, F_{ch-U} : upper and lower chain force.

External forces and torques

- $F_{x-A}, F_{y-A}, F_{z-A}, M_{x-A}, M_{y-A}, M_{z-A}$: aerodynamic forces and torques, applied to the sprung mass,
- $F_{x-F}, F_{y-F}, F_{N-F}$: front tire forces, applied to the front contact mass,
- M_{x-F}, M_{y-F} : front tire torques, applied to the front tire belt,
- $F_{x-R}, F_{y-R}, F_{N-R}$: rear tire forces, applied to the rear contact mass,
- M_{x-R}, M_{y-R} : rear tire torques, applied to the rear tire belt.

1.7 CONCLUSIONS

In this chapter a novel approach to the dynamic modelling of motorcycles was presented. The adopted kinematic description makes it possible to consider forward and lateral road slopes as well as road elevation and to add to the standard motorcycle geometry a rigid-ring tire model without affecting computational efficiency. By means of an independent coordinate formulation it was possible to express the position and orientation of the front wheel axle in the inertial reference frame, reducing the complexity of the resulting expression with respect to the fully relative-coordinate formulations presented in the literature. The selected constraint equations are well defined and continuous for the entire range of feasible motorcycle motions. Moreover, the adopted parametrization yields uncoupled constraint equations, making the evaluation of dependent displacements and velocities computationally inexpensive. On the basis of this kinematic description, a rigid multibody motorcycle model was implemented using a symbolic formalism. The equations of motion were written for the entire set of variables (dependent and independent) using either Lagrange or Newton-Euler equations. The constraint equations were handled using a projection technique, that made it possible to express the dependent variables as a projection of the independent ones over the nullspace of the Jacobian matrix of the constraint equations. As a result, the system of equations of motion was reformulated in terms of independent variables only. Therefore the numerical integration can be performed using a simple ODE algorithm, instead of the DAE algorithm required by conventional formulations (Lagrange multipliers), resulting in a highly enhanced computational efficiency: the developed code is between 3 and 5 times faster than commercial softwares of similar complexity. Moreover, the amount of RAM memory required is extremely low (computation time being influenced mainly by the CPU clock frequency) making the code suitable also for low-capacity computers such as laptops, unlike the majority of commercial softwares.

Some results regarding model validation (numerical vs experimental data) will be presented in chapter 3.

Chapter 2

SHOCK ABSORBER MODEL

2.1 INTRODUCTION

The study of the dynamic behaviour of motorcycle suspensions has been performed via mathematical models of different complexity. The simplest of them is the so-called 2 dofs “quarter car model” [19], which can be studied in closed form under the assumption of linearity of both damping and spring characteristics. While the assumption of spring linearity is not a major limitation (e.g. when coil springs are adopted), it is well known that standard shock absorbers are neither linear nor symmetrical. Hence an “optimal damping” value obtained through a linear model needs corrections, by means of experimental and/or numerical procedures. Experimental tests show that, in a wide range of working conditions (namely in absence of fluid vaporization), the force developed by the damper depends only on the relative velocity of the suspension. This dependency is strongly non-linear [20], due to both purposely built non-linearities, and dry-friction at low speed. Thus a variety of force-velocity characteristics have been proposed, as for example in [21], where the phenomena which contribute to the behaviour of the damper are identified and modelled in detail.

A general force-velocity relation can be expressed in the form [22]:

$$F = f(\dot{z}) = c \cdot \dot{z} + f_e(\dot{z}) + f_o(\dot{z}) \quad (2.1)$$

where \dot{z} is the suspension relative velocity, f_e and f_o are two functions making it possible to model the deviations from symmetry and from linearity. When f_e is linear and f_o vanishes, the function becomes bi-linear and the effect of dry-friction in suspension seals is neglected. The latter can be modelled by an appropriate choice of function f_e . While this approach makes it possible to consider characteristics with complex shapes, it may require different functions for different cartridges and setups, making optimization procedures difficult to approach. Schielen [20] on the other hand proposed a stochastic identification approach, yielding a tri-linear shock function:

$$f(\dot{z}) = \begin{cases} c_3 \cdot (\dot{z} - V_2) + c_1 V_2 & \text{for } \dot{z} > V_2 \\ c_1 \cdot \dot{z} & \text{for } V_1 \leq \dot{z} \leq V_2 \\ c_2 \cdot (\dot{z} - V_1) + c_1 V_1 & \text{for } \dot{z} < V_1 \end{cases} \quad (2.2)$$

where c_1, c_2, c_3 are the angular coefficients of the three linear steps, and V_1, V_2 are reference velocities. This model takes into account the effect of dry-friction, but introduces a non-negligible error in the representation of the damping behaviour at high speed.

In this chapter a different damping characteristic function is proposed, based on a non-parametric B-spline [23]. Its shape is optimized for a cornering maneuver at constant velocity and a braking maneuver over a rough terrain, both simulated by means of a planar multibody non-linear motorcycle model.

2.2 PLANAR MOTORCYCLE MODEL

A simplified planar multibody motorcycle model (with telescopic fork and chain transmission) is considered, as shown in Fig. 2.1. This model features 8 dofs: rear contact point coordinates x and z_r , wheel rotation angles θ_f and θ_r , swingarm pitch angle μ_2 , frame pitch angle μ_3 , fork stroke f_k and drivetrain rotation angle θ_{ds} . The input variables are the front and rear braking torques and the engine torque. Since the model is planar, no steering torque is required. The vertical contact forces with the ground are taken into account with residual stiffness and damping.

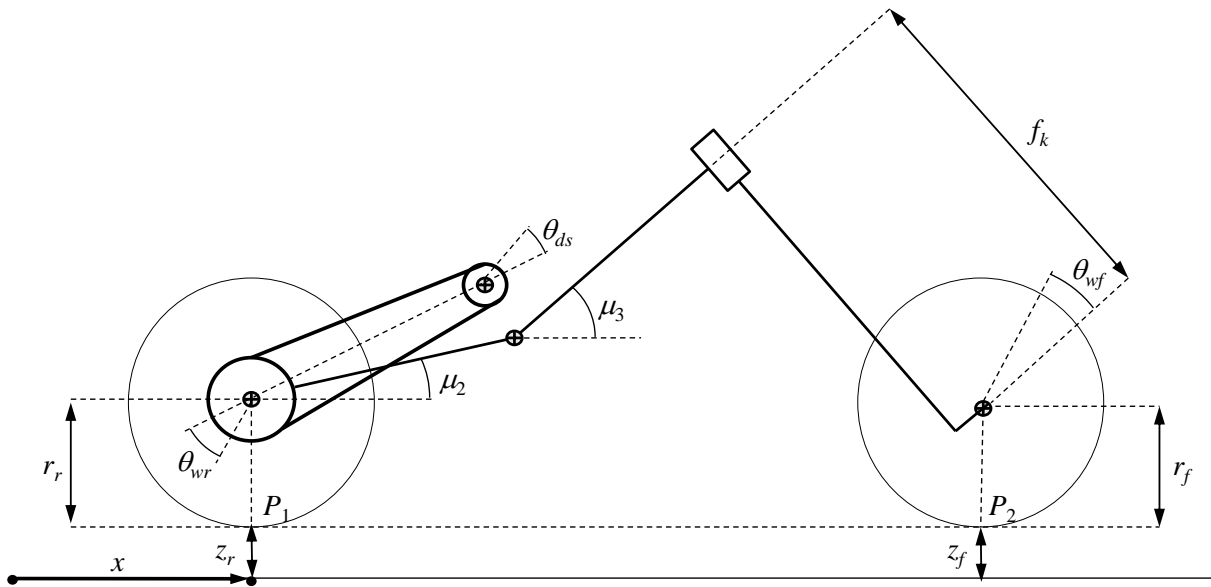


Fig. 2.1: Schematic representation of the adopted (simplified) motorcycle model.

The rear suspension is modelled by a linear-equivalent torsional spring-damper system, taking into account the effects of the rear suspension leverage. The front suspension is modelled by a linear spring in parallel with a non-linear damper, described by a specific function $F_{damp} = f(v)$, where v is the first time derivative of the fork stroke. Since the model is planar, only quasi-steady-state cornering maneuvers can be considered. The in-plane component of the resulting force applied to the mass center G (due to gravity and inertial actions) can be expressed by taking into account also the gyroscopic torques on the wheels:

$$M_i = M_1 + M_2 = \Omega \cos(\phi) \sum_{i=1}^2 J_{0i} \omega_{0i} \quad (2.3)$$

where ϕ is the roll angle, Ω is the cornering angular velocity (i.e. the yaw rate), ω_{0i} and J_{0i} are the angular velocity and the moment of inertia (along the rotation axis) of wheel i , respectively.

Referring to Fig. 2.2, the roll angle can be expressed as:

$$\tan(\phi) = \frac{V^2}{Rg} \left(1 + \frac{1}{mh_G} \sum_{i=1}^2 \frac{J_{0i}}{r_i} \right) \quad (2.4)$$

where V is the motorcycle forward velocity, m its overall mass, h_G the in-plane distance of the mass center from ground, R the cornering radius, r_i the radius of wheel i and g the gravity acceleration. The angle γ is given by:

$$\gamma = \phi - \text{atan} \left(\frac{V^2}{Rg} \right) \quad (2.5)$$

If the gyroscopic effects are neglected, then $\gamma = 0$. The in-plane component of the resulting force applied to the mass center G can be written in the form:

$$F_{in} = \left[mg \sqrt{1 + \left(\frac{V^2}{Rg} \right)^2} \right] \cos(\gamma) \quad (2.6)$$

The input parameters for computing F_{in} are: m , h_G , V , R , r_i and J_{0i} .

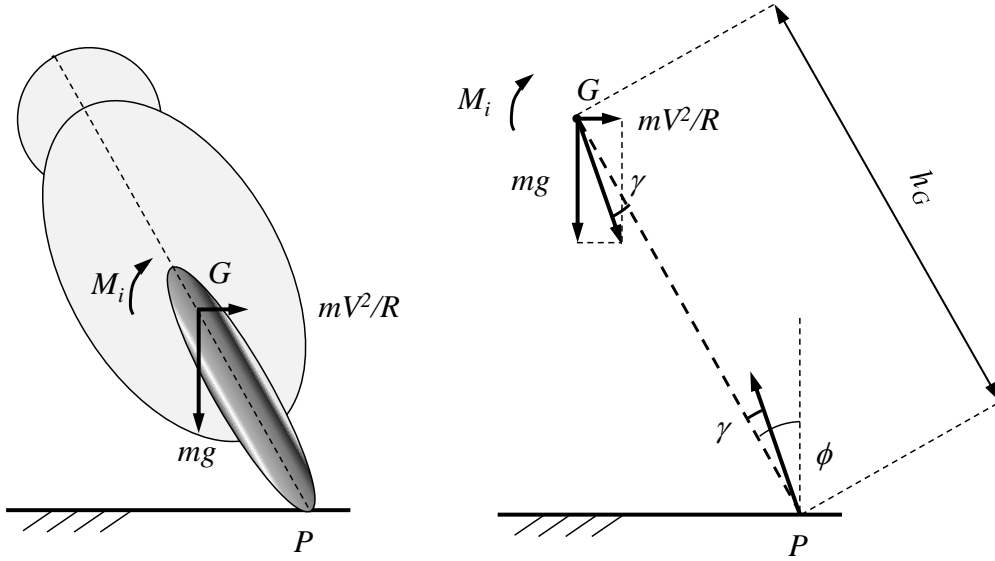


Fig. 2.2: Schematic representation of a motorcycle in steady-state cornering maneuver.

The rolling radiuses of the wheels must be reduced as well. Assuming a torus shaped tire profile gives:

$$r_{eff} = r - \rho[1 - \cos(\phi)] \quad (2.7)$$

where r is the tire radius and ρ is the torus radius. The tire-ground forces are modelled by means of the adherence ellipse, the lateral force being calculated as:

$$F_{yf} = [c_{res}(\dot{y}_{fr} - \dot{z}_f) + k_{res}(y_{fr} - z_f)] \sin(\phi) \quad (2.8)$$

where c_{res} and k_{res} are the values of the linear residual stiffness and damping, z_f is the elevation of the front contact point and y_{fr} is the corresponding road elevation. The whole system is excited with a translating ground displacement applied at the contact points P_1 and P_2 . A ground excitation is applied to the front and rear residual spring-damper systems, with a time-shift depending on the actual wheelbase and on the imposed law of motion. The braking maneuver is performed with an open loop application of a proper braking torque, with the following distribution: 60% front brake, 20% rear brake and 20% engine brake.

2.3 SHOCK ABSORBER MODEL

A set of experimental data supplied by a suspension manufacturer is considered. The experimental characterization was performed by testing the tuning range of different hydraulic cartridges. Figure 2.3 shows the effect of tuning on two different cartridges, taken as an example.

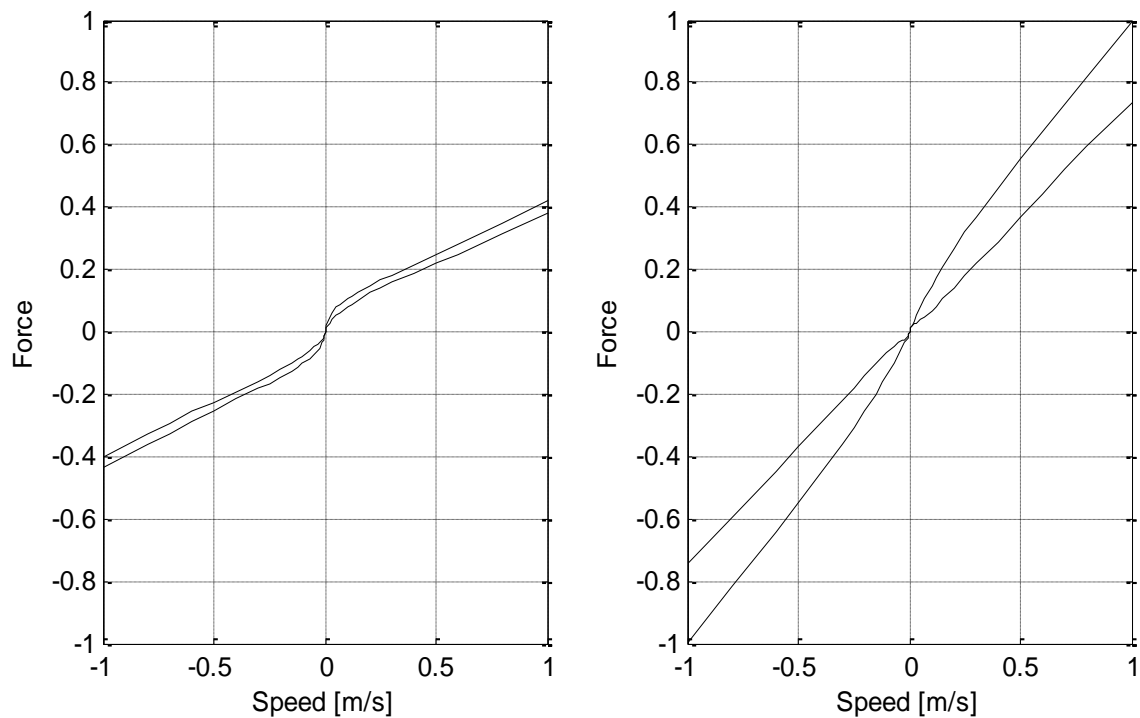


Fig. 2.3: Setup limits for two different cartridges (normalized force values).

The force data are normalized with respect to a reference value. It should be pointed out that the presence of seals produces a dry-friction action for low compression and rebound velocities in the range $[-0.001, 0.001]$ m/s. This makes the cartridge hydraulic contribution negligible, so that the shock behaviour in this velocity range does not vary with respect to any cartridge or tuning setup and shows a linear dependence on shaft speed. The slope of this linear contribution, according the experimental datasets supplied by the manufacturer, is set at:

$$\frac{df}{dv} = 2.5 \cdot 10^4 \quad [\text{Kg} \times \text{s}^{-1}] \quad (2.9)$$

It comes evident from Fig. 2.3 that a tri-linear model cannot reproduce satisfactorily these damping characteristics. Therefore a B-spline model is considered, suitable to model curves of complex shape with a minimum amount of parameters [24]. Let the experimental data be $(v_1, f_1), (v_2, f_2), \dots, (v_s, f_s)$. A generic point belonging to a non-parametric B-spline curve of degree n and r parameters can be expressed as:

$$f(v) = \sum_{k=1}^r N_k^n(v) b_k \quad (2.10)$$

where $N_k^n(v)$ are the spline coefficients, defined over a knot distribution $\mathbf{x} = x_1, \dots, x_{n+r+1}$.

Maximum end knots multiplicity is chosen, that is: $x_1, \dots, x_{n+1} = v_1$ and $x_{r+1}, \dots, x_{r+n+1} = v_s$.

A non-uniform knot distribution is obtained using the optimization algorithm proposed in [25]. Due to the smooth shape of the data sets, the selected degree is $n = 2$. The unknown parameters $b_k = b_1, \dots, b_r$ can be evaluated by solving the system:

$$\begin{Bmatrix} f_1 \\ \vdots \\ f_s \end{Bmatrix} = \begin{bmatrix} N_1^n(v_1) & \cdots & N_r^n(v_1) \\ \vdots & \ddots & \vdots \\ N_1^n(v_s) & \cdots & N_r^n(v_s) \end{bmatrix} \begin{Bmatrix} b_1 \\ \vdots \\ b_r \end{Bmatrix} \Leftrightarrow \mathbf{f} = \mathbf{N} \cdot \mathbf{b} \quad (2.11)$$

If the number of parameters r equals the number of given data s , there would be interpolation. This case is not convenient for the present application, since a relatively low number of parameters ($r \ll s$) yields a low number of optimization dofs, and oscillations between fitted points should not arise. On the other hand, lowering the number of parameters and solving the over determined system in the least square sense would lead to ignore the dry-friction effect.

In order to provide a precise representation also in the region in which the dry-friction dominates, with a minimum number of parameters, the system Eq. (2.11) is partitioned into two sub-systems:

$$\begin{cases} f_1 \\ \vdots \\ f_m \\ f_{m+1} \\ \vdots \\ f_s \end{cases} = \begin{bmatrix} N_1^n(v_1) & \cdots & N_r^n(v_1) \\ \vdots & \ddots & \vdots \\ N_1^n(v_m) & \cdots & N_r^n(v_m) \\ N_1^n(v_{m+1}) & \cdots & N_r^n(v_{m+1}) \\ \vdots & \ddots & \vdots \\ N_1^n(v_s) & \cdots & N_r^n(v_s) \end{bmatrix} \begin{cases} b_1 \\ \vdots \\ b_r \end{cases} \Leftrightarrow \begin{cases} \mathbf{f}_I \\ \mathbf{f}_{II} \end{cases} = \begin{bmatrix} \mathbf{N}_I \\ \mathbf{N}_{II} \end{bmatrix} \cdot \mathbf{b} \quad (2.12)$$

Matrix \mathbf{N}_I has dimension $m \times r$ and matrix \mathbf{N}_{II} has dimension $(s - m) \times r$. It is well known that the SVD technique allows any $m \times n$ real matrix \mathbf{A} to be factorized in the form $\mathbf{A} = \mathbf{U}\mathbf{\Sigma}\mathbf{V}$ where \mathbf{U} is a $m \times m$ orthogonal matrix, \mathbf{V} is an $n \times n$ orthogonal matrix and $\mathbf{\Sigma}$ is a $m \times n$ diagonal matrix with $\sigma_{ii} = \sigma_i \geq 0$ [26]. Applying the SVD to the system Eq. (2.12) yields:

$$\begin{cases} \mathbf{N}_I \cdot \mathbf{b} = \mathbf{f}_I \\ \mathbf{N}_{II} \cdot \mathbf{b} = \mathbf{f}_{II} \end{cases} \Rightarrow \begin{cases} \mathbf{U}_I \mathbf{\Sigma}_I \mathbf{V}_I \cdot \mathbf{b} = \mathbf{f}_I \\ \mathbf{U}_{II} \mathbf{\Sigma}_{II} \mathbf{V}_{II} \cdot \mathbf{b} = \mathbf{f}_{II} \end{cases} \Rightarrow \begin{cases} \mathbf{\Sigma}_I \mathbf{V}_I \cdot \mathbf{b} = \mathbf{U}_I^T \cdot \mathbf{f}_I \\ \mathbf{\Sigma}_{II} \mathbf{V}_{II} \cdot \mathbf{b} = \mathbf{U}_{II}^T \cdot \mathbf{f}_{II} \end{cases} \quad (2.13)$$

Introducing two new variables \mathbf{Z}_I and \mathbf{Z}_{II} , their p -th and q -th components can be computed as follows:

$$\begin{aligned} \mathbf{Z}_I = \mathbf{V}_I \cdot \mathbf{b} &\Rightarrow (\mathbf{Z}_I)_p = \frac{(\mathbf{U}_I^T \cdot \mathbf{f}_I)_p}{(\sigma_I)_p} \quad \text{for } p = 1, \dots, m \\ \mathbf{Z}_{II} = \mathbf{V}_{II} \cdot \mathbf{b} &\Rightarrow (\mathbf{Z}_{II})_q = \frac{(\mathbf{U}_{II}^T \cdot \mathbf{f}_{II})_q}{(\sigma_{II})_q} \quad \text{for } q = 1, \dots, s - m \end{aligned} \quad (2.14)$$

All the m components of vector \mathbf{Z}_I are considered, and collected in a new vector $\bar{\mathbf{Z}}_I$. Only the first $r - m$ components of vector \mathbf{Z}_{II} are considered, and collected in a new vector $\bar{\mathbf{Z}}_{II}$. Consequently, the dimension of $\bar{\mathbf{Z}}_I$ is $m \times 1$ and the one of $\bar{\mathbf{Z}}_{II}$ is $(r - m) \times 1$. Hence:

$$\begin{cases} \bar{\mathbf{Z}}_I = \bar{\mathbf{V}}_I \cdot \mathbf{b} \\ \bar{\mathbf{Z}}_{II} = \bar{\mathbf{V}}_{II} \cdot \mathbf{b} \end{cases} \quad (2.15)$$

where $\bar{\mathbf{V}}_{\text{I}}$ and $\bar{\mathbf{V}}_{\text{II}}$ are obtained from \mathbf{V}_{I} and \mathbf{V}_{II} by including only the first m and $r-m$ rows. So $\bar{\mathbf{V}}_{\text{I}}$ and $\bar{\mathbf{V}}_{\text{II}}$ have dimensions $m \times r$ and $(s-m) \times r$. Merging vectors $\bar{\mathbf{Z}}_{\text{I}}$ and $\bar{\mathbf{Z}}_{\text{II}}$ with matrices $\bar{\mathbf{V}}_{\text{I}}$ and $\bar{\mathbf{V}}_{\text{II}}$ the following system of r equations in r unknowns can be obtained:

$$\begin{bmatrix} \bar{\mathbf{V}}_{\text{I}} \\ \bar{\mathbf{V}}_{\text{II}} \end{bmatrix} \cdot \mathbf{b} = \begin{Bmatrix} \bar{\mathbf{Z}}_{\text{I}} \\ \bar{\mathbf{Z}}_{\text{II}} \end{Bmatrix} \quad (2.16)$$

It is now possible to determine the vector \mathbf{b} (unknown spline parameters):

$$\mathbf{b} = \begin{bmatrix} \bar{\mathbf{V}}_{\text{I}} \\ \bar{\mathbf{V}}_{\text{II}} \end{bmatrix}^{-1} \cdot \begin{Bmatrix} \bar{\mathbf{Z}}_{\text{I}} \\ \bar{\mathbf{Z}}_{\text{II}} \end{Bmatrix} \quad (2.17)$$

The first m equations are selected to interpolate the damping behaviour due to friction in the velocity range $[-0.001, 0.001]$ m/s. The minimum number of parameters for this purpose is $m = 3$, hence the conditions are set to $f(-0.001) = -25$ N, $f(0) = 0$, $f(0.001) = 25$ N.

Numerical tests led to the use of other six parameters for a least square fitting of the remaining experimental data. Hence the total number of unknown parameters becomes $r = 9$. This procedure is repeated for every measured shock dataset, making it possible to identify an optimal knot sequence and set of parameters for each dataset. A final knot sequence is thus computed averaging all of the optimal knot sequences for every dataset in order to minimize the modelling error through the entire range of different cartridge models, and associated feasible adjustments.

The actual comparison between experimental data and spline-modelled data is shown in Fig. 2.4, where red dots represent the experimental data, cyan solid lines represent the fully-interpolated experimental data, blue lines represent the B-spline modelled data and green squares represent the Greville abscissae for the proposed B-splines. A close-up view in the range dominated by the effect of dry-friction is shown in Fig. 2.5, in order to show the effectiveness of the proposed method.

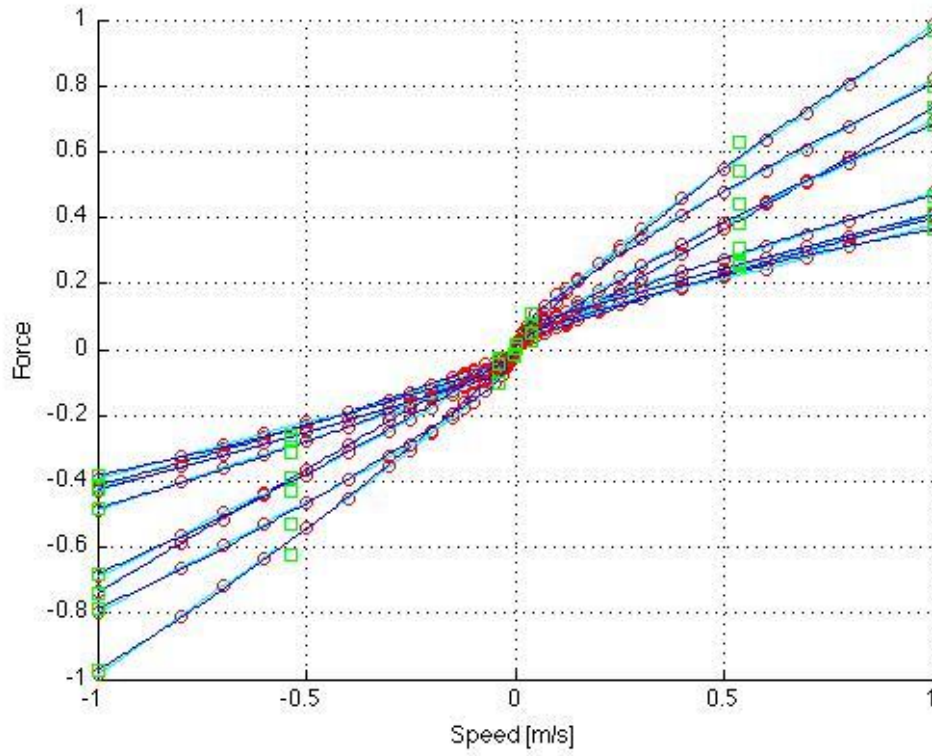


Fig. 2.4: Comparison between experimental data and proposed model.

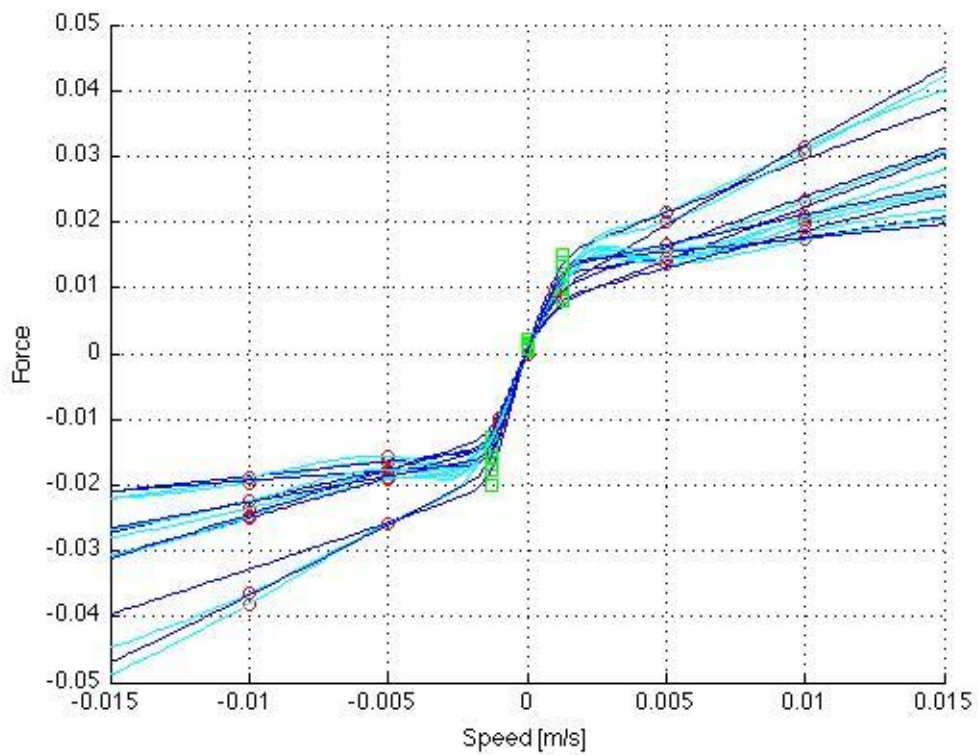


Fig. 2.5: Comparison between experimental data and proposed model (dry friction effect).

2.4 GROUND ROUGHNESS MODEL

Experimental measurements show that the actual road roughness can be described by a Gaussian, ergodic and stationary random process with zero mean value. Road quality is defined by the frequency content of the surface elevation. A standard model [27] for defining the ground power spectral density (PSD) from measured data is:

$$S_y(\Omega) = S_0 \left(\frac{\Omega_0}{\Omega} \right)^w \quad \text{with} \quad 0 < \Omega_1 \leq \Omega \leq \Omega_2 < \infty \quad (2.18)$$

with reference spatial frequency $\Omega_0 = 1$ rad/m and exponent $w = 2$ for constant speed PSD. The spectral density $S_\xi(\Omega)$ for the spatial frequency between $0 \leq \Omega < \Omega_1$ and $\Omega > \Omega_2$ shows a minor influence on the dynamic behaviour of vehicles [27]. Therefore the spectral density $S_\xi(\Omega)$ is usually assumed to be constant on both spatial frequency ranges:

$$\begin{aligned} S_y(\Omega) &= S_y(\Omega_1) && \text{for } 0 \leq \Omega < \Omega_1 \\ S_y(\Omega) &= 0 && \text{for } \Omega > \Omega_2 \end{aligned} \quad (2.19)$$

The following parameters are typical for a smooth A-class road: $\Omega_1 = 0.05$ rad/m, $\Omega_2 = 500$ rad/m, $S_0 = 4.68 \cdot 10^{-6}$ m²/(rad/m). The generation of a sample function of a stochastic process plays a major role in road surface simulation. For this purpose the spectral representation method described in [28] is adopted. It has been shown that the ensemble and temporal autocorrelation functions for a fixed time lag τ converge to their target autocorrelation function as $n \rightarrow \infty$. The simulation formula is:

$$y(t) = \sqrt{2 \sum_{n=0}^{N-1} A_n \cos(\omega_n t + \varphi_n)} \quad (2.20)$$

where $\varphi_n (n=0,1,\dots,N-1)$ are independent random phase angles uniformly distributed in the range $[0,2\pi]$. The frequencies are set to $\omega_n = n\Delta\omega = n \frac{\omega_u}{N} = n \frac{2\pi}{T}$, where T is the simulation total time. The coefficients A_0 and A_n for $n=1,2,\dots,N-1$ are defined as follows:

$$\begin{aligned} A_0 &= 0 \\ A_n &= \sqrt{2S_\xi(\omega_n)\Delta\omega} \end{aligned} \quad (2.21)$$

The coefficient A_0 is set equal to zero, as the mean value averaged over the entire simulation time of the generated stochastic process remains zero. The data are sampled from the initial time $t_0 = 0$ to the final time $T = 32.768$ s with a time step $\Delta t = 0.001$ s and $N = 2^{15}$ samples. Since the computed road elevation does not match the measured data for racetracks, a scaling factor $sf = 0.3$ has been adopted. A realization of the stochastic ground roughness is shown in Fig. 2.6.

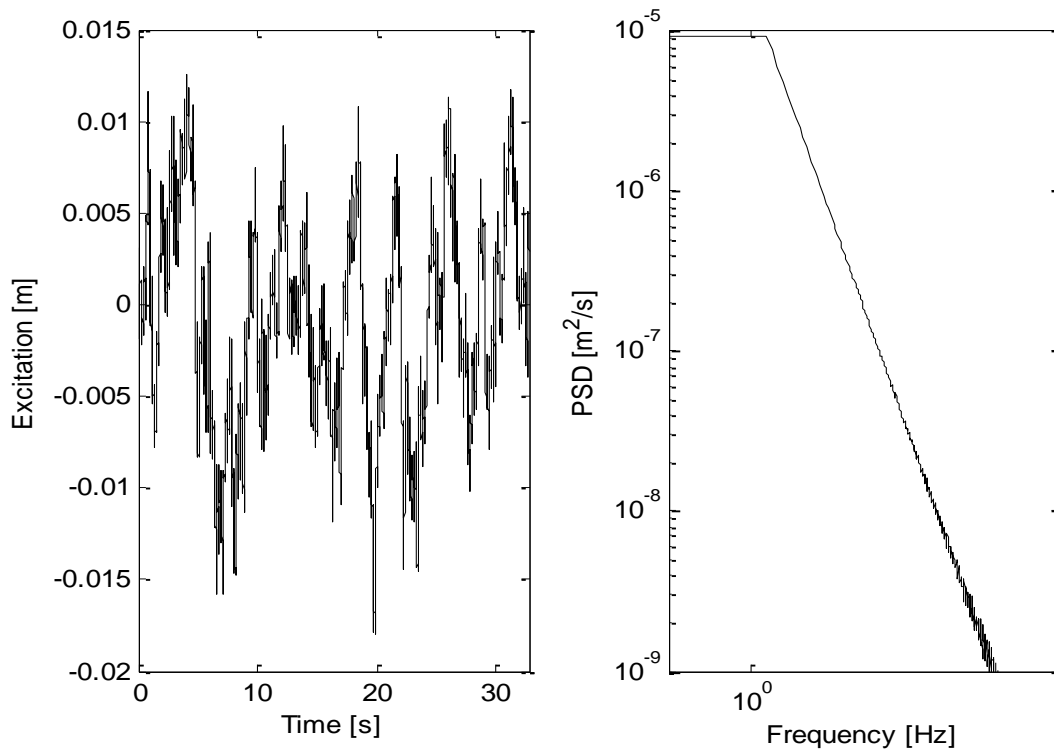


Fig. 2.6: A realization of the stochastic ground roughness for $V=100$ km/h.

2.5 TWO DIFFERENT MANEUVERS

Two different maneuvers are considered, as shown in Fig. 2.7, and numerically integrated in the time domain with time-step $\Delta t = 0.001$. The first one is a constant velocity maneuver at speed $V = 180$ km/h over the terrain described in section 2.4, with an imposed constant roll angle $\phi = 50^\circ$. The second one is a braking maneuver, starting at $V = 300$ km/h with constant deceleration $a_x = -5$ m/s², ending after 10 s at a speed $V = 100$ km/h, over the same terrain.

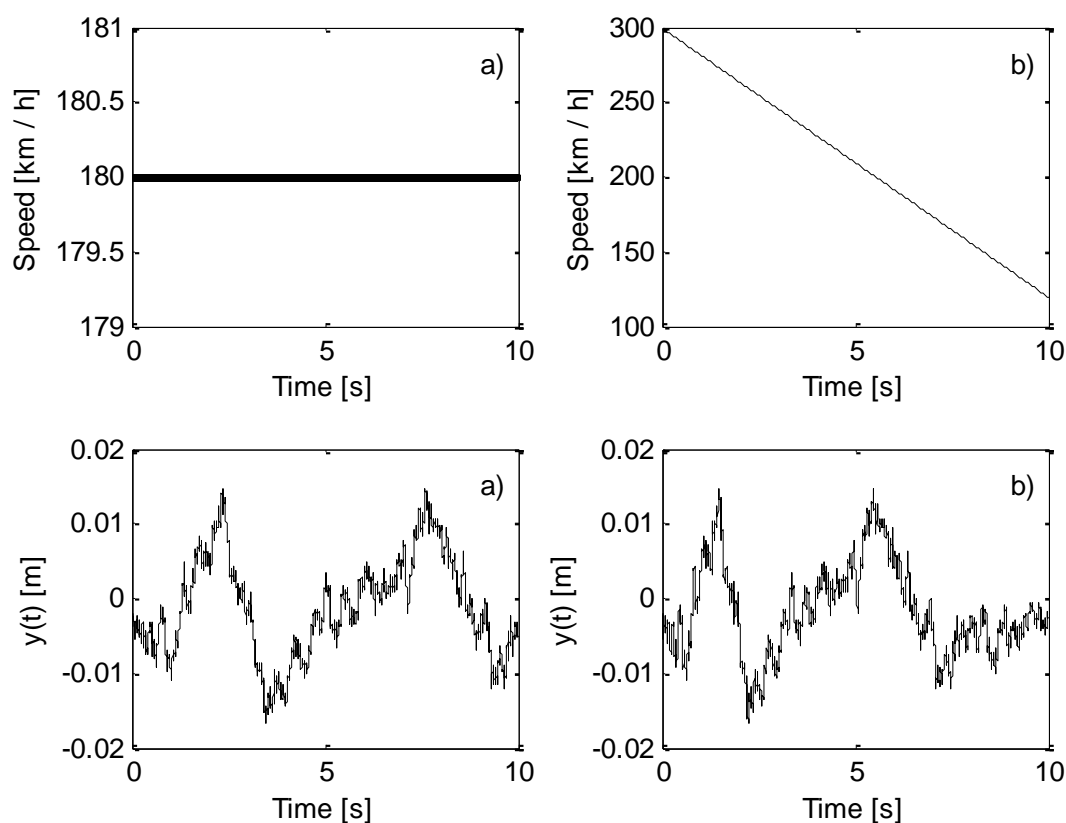


Fig. 2.7: (left) Constant speed maneuver and relative ground displacement; (right) braking maneuver and respective ground displacement.

2.6 OPTIMIZATION OBJECTIVE FUNCTION

The vehicle performance generally depends on the longitudinal traction forces, the braking forces and the lateral guidance forces between tires and ground [29]. These forces are essentially influenced by the normal load acting in the tire contact area. The normal load outlines a contribution due to the vehicle weight and a dynamic contribution due to vehicle

vibration. Since the relation between contact forces and normal load is strongly nonlinear [4], even small variations in wheel load can significantly worsen the overall vehicle performance. Hence the optimal suspension system, with respect to a performance index, may be the one that minimizes the dynamic component of the wheel load [29].

For an assessment of vehicle performance, the RMS value of the normal front tire force is considered, as the front tire adherence represents the main performance limiting factor for the considered maneuvers. The normal front tire force F_{z_f} is given by:

$$F_{z_f} = \left[c_{res} (\dot{y}_{fr} - \dot{z}_f) + k_{res} (y_{fr} - z_f) \right] \cos(\phi) \quad (2.22)$$

Therefore a normalized objective function is proposed in the form of:

$$obj = \frac{RMS(F_{z_f})}{RMS(F_{z_f0})} \quad (2.23)$$

where F_{z_f0} is the front tire force computed in case of absence of front suspension damping in a reference condition, that is the static trimming condition.

Two penalization terms are added to the above objective function. The first penalization term is added in order to reject the damping setups allowing the front tire detachment from the ground. This term is non-null if $F_{z_f} < 0$, that is when the front tire is not in contact with the ground, and it is defined as:

$$\begin{aligned} pn_1 &= -c_1 \cdot \min(F_{z_f}) / F_{stat} & \text{if } F_{z_f} < 0 \\ pn_1 &= 0 & \text{if } F_{z_f} \geq 0 \end{aligned} \quad (2.24)$$

where c_1 is a numerical coefficient chosen w.r.t. the overall penalty function value and F_{stat} is the front wheel load in static condition.

The second penalization term is added in order to reject the damping setups originating unwanted and potentially dangerous sprung-mass oscillations. In Fig. 2.8 the modulus of the Fourier transform of the front suspension stroke f_k in the case of null front suspension damping and null longitudinal acceleration is shown.

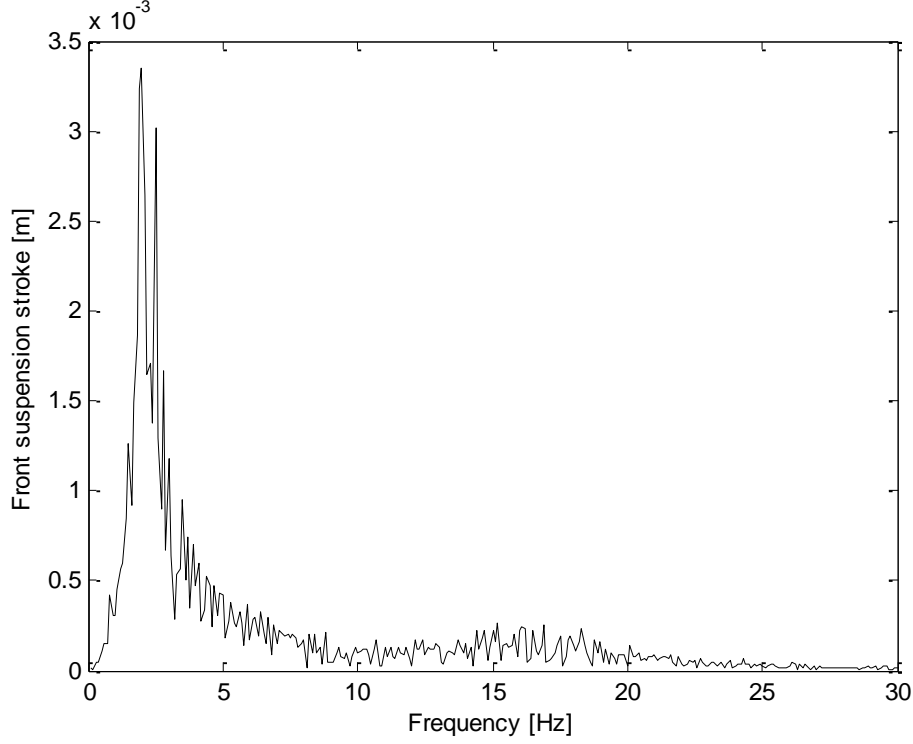


Fig. 2.8: Fourier transform of the front suspension stroke.

A peak is evident in correspondence of 3 Hz, this value being close to the first natural frequency of the linearized model in the vehicle static kinematical configuration. Those natural frequencies are associated with the modes of sprung mass, vertical bounce and sprung mass pitch, that become unstable for low values of front suspension damping, resulting in performance limiting sprung mass oscillation during the maneuver. Hence a penalty term is defined as:

$$pn_2 = \frac{R}{R_0} \quad (2.25)$$

where R is the actual RMS value of front suspension stroke Fourier transform in the frequency range $f \in [2.5, 4]$ Hz and R_0 is the analogous, computed in case of no front suspension damping. Hence the new objective function is defined as:

$$obj_{fm} = obj + pn_1 + pn_2 \quad (2.26)$$

The optimal damping characteristic is the one that minimizes this objective function. Optimization is now held for the constant speed maneuver and the braking maneuver. Only six of the nine spline parameters b_k are chosen as optimization variables. The three parameters b_4 , b_5 , b_6 describing the dry friction behaviour are hold fixed, since the experimental data from the suspension manufacturer (see Fig. 2.5) show that $f(v)$ displays only slight differences in the range $v \in [-0.001, 0.001]$ m/s with respect to different damping cartridges and tuning setups.

2.7 OPTIMIZATION RESULTS

The initial conditions for the optimization algorithm are displayed in Fig. 2.9, along with the boundaries of the optimization field.

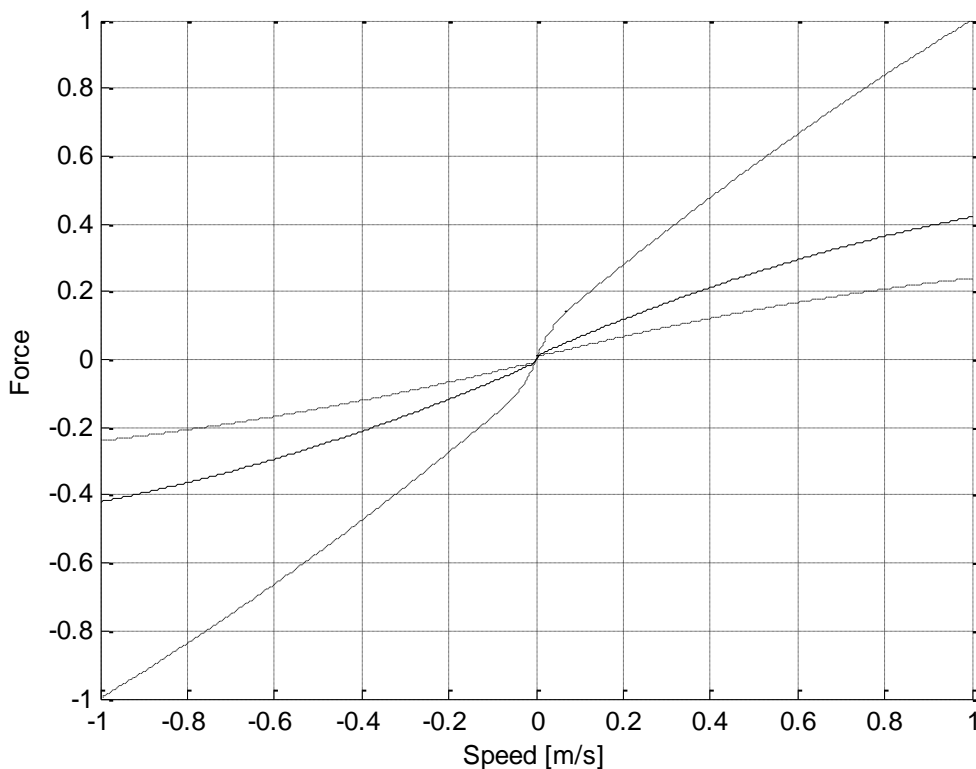


Fig. 2.9: Optimization boundaries (dash-dot lines) and initial condition (solid line).

Figure 2.10-left shows the optimal characteristic curve for the constant speed maneuver (see Fig. 2.7-left). In Fig. 2.10 the velocity interval reproduce the the range of suspension speeds obtained in the numerical simulation of the maneuver.

Figure 2.10-right shows the optimal characteristic curve for the braking maneuver (see Fig. 2.7-right). Both optimal damping characteristics display a similar shape for compression stroke: an increase in compression damping force with respect to the optimization initial values. On the other hand, the optimal damping curve for the constant speed cornering maneuver shows a lower speed rebound force in comparison with the optimal one for the braking maneuver.

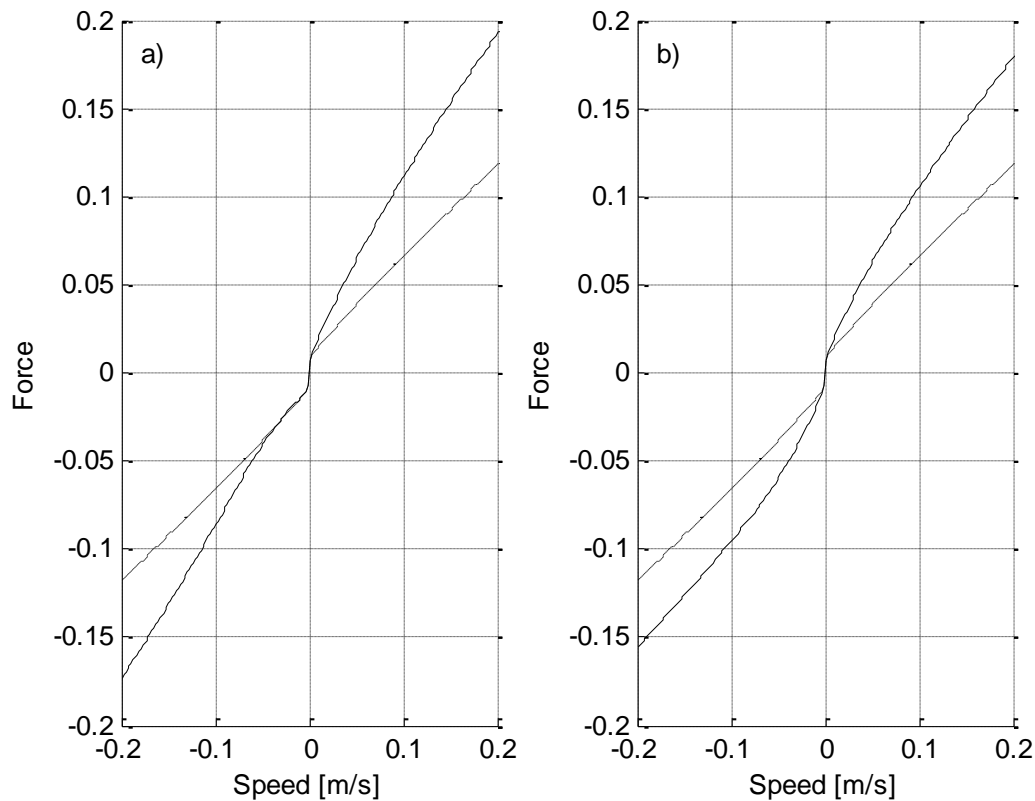


Fig. 2.10: (left) Optimal damping characteristic for constant speed maneuver (solid line) and optimization initial condition (dash-dot line); (right) Optimal damping characteristic for braking maneuver (solid line) and optimization initial condition (dash-dot line).

The optimization results obtained using the above procedure applied to a simpler, half-car vehicle model, can be found in [30].

2.8 CONCLUSIONS

In this chapter a handling-oriented procedure was presented for the optimization of a suspension damping characteristic. A set of experimentally measured damper diagrams were modelled with a non-parametric B-spline curve. In order to keep into account the dry-friction and all of the tuning setup effects, a procedure for determining the spline parameters was defined and adopted. Part of the spline parameters, used to fit experimental damper measurements, were computed by means of interpolation of experimental data, while the remaining ones were obtained by means of least square fitting, and only six independent parameters were selected to model all of the different cartridges and tuning setups. A handling-oriented objective function for optimization was defined, considering the wheel-ground contact conditions and the whole vehicle dynamic behaviour. Two applications, concerning the simulation of a cornering maneuver and a braking maneuver were considered, and their associated “optimal” cartridge characteristics were found.

Chapter 3

A SIMPLIFIED PLANAR MODEL FOR THE ANALYSIS OF MOTORCYCLE CHATTERING

3.1 INTRODUCTION

In [31] a self-excited vibration was simulated, consistent with the actual chatter vibration of road racing motorcycles. It has been shown how the interaction between chain force, rear suspension motion and tire radial deformability is the driving mechanism for the self-excitation, in case of rear longitudinal relaxation length dependent of vertical load. In order to analyze in detail the coupling between tire radial deformation, chain transmission and tire relaxation behaviour, a simplified planar model is developed in this chapter. Considering a planar model makes it possible to develop an analytical approach to the chatter vibration without loss of generality, since this phenomenon takes place in the motorcycle midplane and in stationary cornering conditions (after brake release and before throttle application). The simplified system consists of a radially deformable lenticular wheel moving over flat surface, suspended with respect to a forward moving frame. The vertical guidance system of the wheel axle is tilted by an angle α , close to the swingarm angle of the actual motorcycle in cornering trim. It was demonstrated experimentally by Prof. S.K. Clark at the University of Michigan in 1970 that an unstable oscillatory mode may indeed show up for this system. In [32] Prof. Pacejka proved analytically how the stability of this motion is determined by the coupling between rolling radius and vertical ground load. Starting from the model developed in [32] (reported also in [4]), modifications are made in order to take into account the interaction of the chain braking force in the simplest possible way, to show instability occurrence due to chain interaction. The effects of a braking torque and of damping are considered as well. After presenting the constitutive and equilibrium (simplified) linearized equations of the model, the characteristic equation is derived in a dimensionless form. Some numerical results are discussed by means of root-loci and stability maps, computed by applying the Hurwitz criterion. Finally, some remarks are included, regarding the constitutive model of the longitudinal slip force.

3.2 PLANAR MODEL

The planar linear model considered in this chapter is represented in Fig. 3.1. For the sake of clarity, the nomenclature adopted in the analytical developments presented in this chapter is summarized in Tab. 3.1.

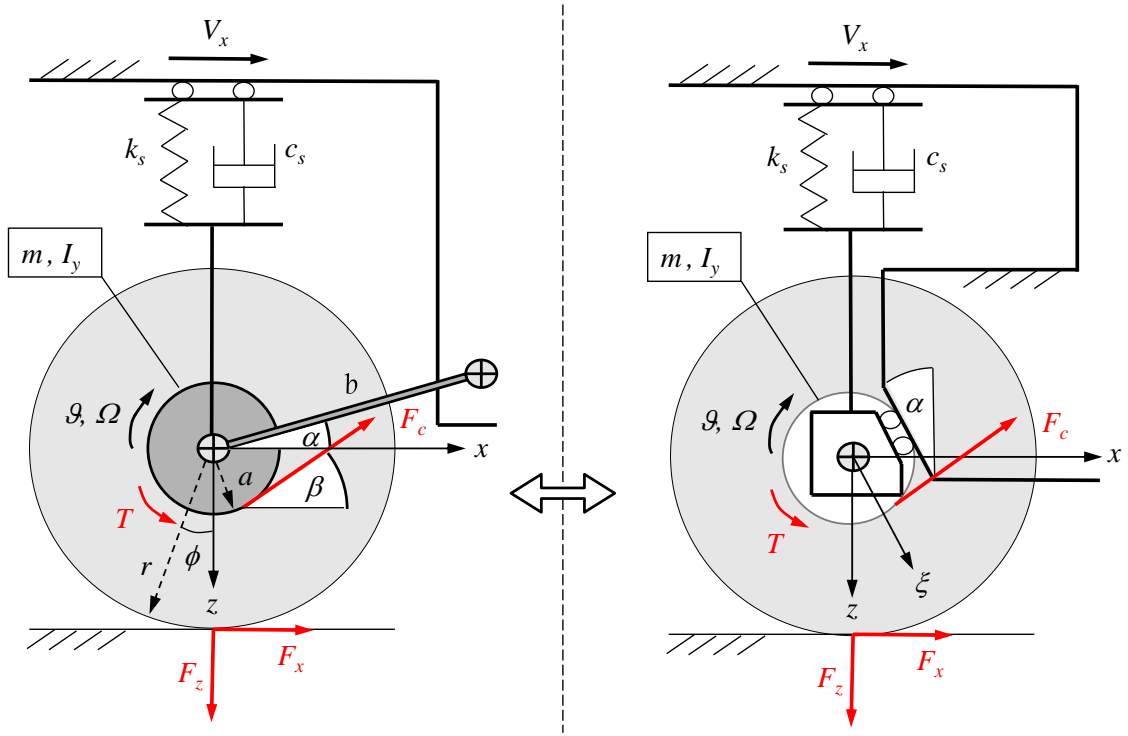


Fig. 3.1: Planar wheel and chain transmission model.

Displacements	Stiffness parameters	Dimensional parameters
ξ displacement of the axle $z = \xi \cos \alpha$ vert. displ. of the axle $x = \xi \sin \alpha$ $x = z \tan \alpha$ } long. displ. of the axle ϑ angular displ. of the rim $\Omega = \dot{\vartheta}$ angular vel. of the rim ϕ torsion angle of the tire $u = \phi r_e$ displ. of the contact point	k_s stiffness of the suspension k_c stiffness of the chain C_z vert. stiffness of the tire C_x ground stiff. of the tire C_{κ} longitudinal slip stiffness	r free outer radius of the wheel r_e effective rolling radius a radius of the chainwheel b length of the swingarm V_x longitudinal speed of the axle $V_{sx} = V_x - r_e \Omega$ longitudinal slip speed $\kappa = -V_{sx} / V_x$ longitudinal slip $\sigma_x = C_{\kappa} / C_x$ relaxation length
	Damping parameters	
	c_s damping of the suspension	
Forces	Inertial parameters	Dimensionless parameters
$F_x = -C_x r \phi$ longitudinal force $F_z = -C_z z$ vertical force $F_c = -k_c a \vartheta$ chain force T braking torque	m eq. mass (wheel + swingarm) $m_r = m / \cos^2 \alpha$ eq. mass (z -dir.) I_y moment of inertia (wheel)	α angle of the swingarm β angle of F_c η deflection parameter of the tire p coupling parameter for F_c

Tab. 3.1: Nomenclature adopted in this chapter.

The linearized constitutive and equilibrium equations are written next in a simplified form neglecting the rolling resistance, the coupling term $z \cdot \sin(\beta)$, approximating r_e with r , and introducing a parameter p (either positive or negative, $|p| < 1$) for describing the coupling between the chain force F_c and the suspension compression. These equations in the time domain read:

$$\begin{cases} m_r \ddot{z} + c_s \dot{z} + k_s z = pk_c a \mathcal{G} + F_z + F_x \tan \alpha \\ I_y \ddot{\mathcal{G}} + k_c a^2 \mathcal{G} = -T - r F_x \\ \left[\frac{\sigma_\kappa}{V_x} \dot{F}_x + F_x \right] = \frac{C_\kappa}{V_x} \left\{ r \dot{\mathcal{G}} - \left[\dot{x} + (1-\eta) \frac{V_x}{r} z \right] \right\} \end{cases} \quad (3.1)$$

The first equation is the vertical equilibrium of the mass m_r , the second one is the rotational equilibrium of the rim, while the last one is the linearized constitutive equation for the non-steady-state longitudinal slip force F_x , as obtained by Pacejka [32]: note that linear dependency of F_x on z vanishes if $\eta \rightarrow 1$.

The expressions of x and F_z as linear functions of z , as reported in Tab. 3.1, can be introduced in the constitutive and equilibrium equations, rewritten in the complex Laplace domain as follows (using the same symbols for the transforms of z , \mathcal{G} , F_x and T):

$$\begin{cases} (m_r s^2 + c_s s + k_s + C_z) z = pk_c a \mathcal{G} + F_x \tan \alpha \\ (I_y s^2 + k_c a^2) \mathcal{G} = -T - r F_x \\ \left[\left(\frac{\sigma_\kappa}{V_x} s + 1 \right) F_x \right] = \frac{C_\kappa}{V_x} \left\{ r s \mathcal{G} - \left[s \tan \alpha + (1-\eta) \frac{V_x}{r} z \right] \right\} \end{cases} \quad (3.2)$$

After eliminating the variables \mathcal{G} and F_x , setting $T = 0$ yields the characteristic equation in the form of a 5th order polynomial P :

$$P(s_n) = A_5 s_n^5 + A_4 s_n^4 + A_3 s_n^3 + A_2 s_n^2 + A_1 s_n + A_0 = 0 \quad (3.3)$$

which can be written in dimensionless form by introducing some characteristic angular frequencies and related ratios, as in [32]:

$$\left\{ \begin{array}{l} \omega_z^2 = \frac{k_s + C_z}{m_r} \quad \text{vertical (bounce)} \\ \omega_\phi^2 = \frac{C_x r^2}{I_y} \quad \text{torsional (wheel)} \\ \omega_g^2 = \frac{k_c a^2}{I_y} \quad \text{torsional (rim + chain)} \end{array} \right. \Rightarrow \left\{ \begin{array}{l} s_n = \frac{s}{\omega_z} \\ \tau_\phi = \frac{\omega_\phi^2}{\omega_z^2} \\ \tau_g = \frac{\omega_g^2}{\omega_z^2} \end{array} \right. \quad (3.4)$$

as well as some other dimensionless parameters:

$$\left\{ \begin{array}{l} \zeta = \frac{c_s}{2m_r \omega_z} \quad \text{damping ratio} \\ \sigma_x = \frac{C_x}{k_s + C_z} \quad \text{longitudinal / vertical stiffness ratio} \\ \gamma = \frac{C_\kappa}{r C_x} = \frac{\sigma_\kappa}{r} \quad \text{normalized relaxation length} \\ V_{nx} = \frac{V_x}{r \omega_z} \quad \text{normalized longitudinal speed of the axle} \\ \Delta = \tan \alpha - p \frac{r}{a} \quad \text{geometrical coupling parameter} \end{array} \right. \quad (3.5)$$

Then the coefficients A in polynomial P take the form:

$$\begin{aligned} A_5 &= 1; \quad A_4 = \frac{V_{xn}}{\gamma} + 2\zeta; \quad A_3 = 1 + \tau_\phi + \tau_g + \sigma_x \tan^2 \alpha + 2\zeta \frac{V_{xn}}{\gamma} \\ A_2 &= \frac{V_{xn}}{\gamma} [1 + \tau_g + (1 - \eta) \gamma \sigma_x \tan \alpha] + 2\zeta (\tau_\phi + \tau_g) \\ A_1 &= \tau_\phi + \tau_g \left(1 + \Delta \sigma_x \tan \alpha + 2\zeta \frac{V_{xn}}{\gamma} \right); \quad A_0 = \tau_g \frac{V_{xn}}{\gamma} [1 + \tau_g + (1 - \eta) \gamma \Delta \sigma_x] \end{aligned} \quad (3.6)$$

in the case $\tau_g = 0$ (i.e. $k_c = 0$) and $\zeta = 0$, the coefficients of P reduce exactly to those of the model studied by Pacejka [32]; the coupling parameter Δ can be either positive or negative,

but given the rear suspension kinematics of a road racing motorcycle its modulus is small and it holds that $|\Delta| < 1$;

P is a 5th order polynomial due to the interaction of the chain force F_c ; otherwise P would have been a 4th order polynomial (as in the case studied by Pacejka [32]), with two couples of complex-conjugate eigenvalues corresponding to the modes of vertical and rotational displacement. The presence of the chain interaction produces one more real negative eigenvalue, since the constitutive model of F_x , (actually a Maxwell model), consisting of a series of a spring C_x and a damper C_κ/V_x , becomes a Zener model by addition of one more spring in parallel, i.e. k_c .

When $C_x \rightarrow \infty$ (with $k_c = 0$), the Maxwell model reduces to a Newton one (single damper), the relaxation length $\sigma_\kappa \rightarrow 0$, the differential expression of F_x becomes algebraic and the characteristic equation P reduces to a 3rd order polynomial (a couple of complex-conjugate eigenvalues, plus a real one). This reduction leads to a non-realistic model, that is a tire without torsional deformability. On the contrary, in the case of the rigid-ring model described in chapter 1, even letting the residual longitudinal stiffness $C_x \rightarrow \infty$, the torsional stiffness of the tire is still present, and it is given by the rotational stiffness between belt and rim.

3.3 STABILITY ANALYSIS

Root-loci and stability maps are computed varying the values of the following parameters: α , γ , ζ and Δ , while the following dimensionless parameters are hold fixed according to the assumptions made by Pacejka [32]:

$$\tau_\phi = 16, \quad \tau_g = 2\tau_\phi, \quad \sigma_x = 2.5, \quad \eta = 2/3, \quad V_{nx} = 1 \quad (3.7)$$

While in the model proposed by Pacejka (without chain interaction) the instability arises first for the rotational mode, when considering F_c the first potentially unstable mode becomes the vertical one (bounce).

The root-loci shown in Fig. 3.2 are related to the vertical mode eigenvalue with negative imaginary part. Note that, having the eigenvalues been normalized with respect to ω_c , in this case if $\text{Re}(s_n) \rightarrow 0$, then $|\text{Im}(s_n)| \rightarrow 1$.

The plots are computed by varying Δ (either from 0 to + 0.3, or from 0 to – 0.3) for two different values of α (10° and 18°) and two different values of γ (0.2 and 0.5), while keeping $\zeta = 0$. Note that if $\Delta = 0$, the root s_n is not exactly in $(0, -1)$.

For $\Delta \rightarrow +0.3$, $\text{Im}(s_n) < -1$, while for $\Delta \rightarrow -0.3$, $\text{Im}(s_n) > -1$.

For $\Delta < 0$, the system can be stabilized either by reducing α , or by increasing γ . And vice-versa for $\Delta > 0$. This behaviour can be clarified by drawing some stability maps.

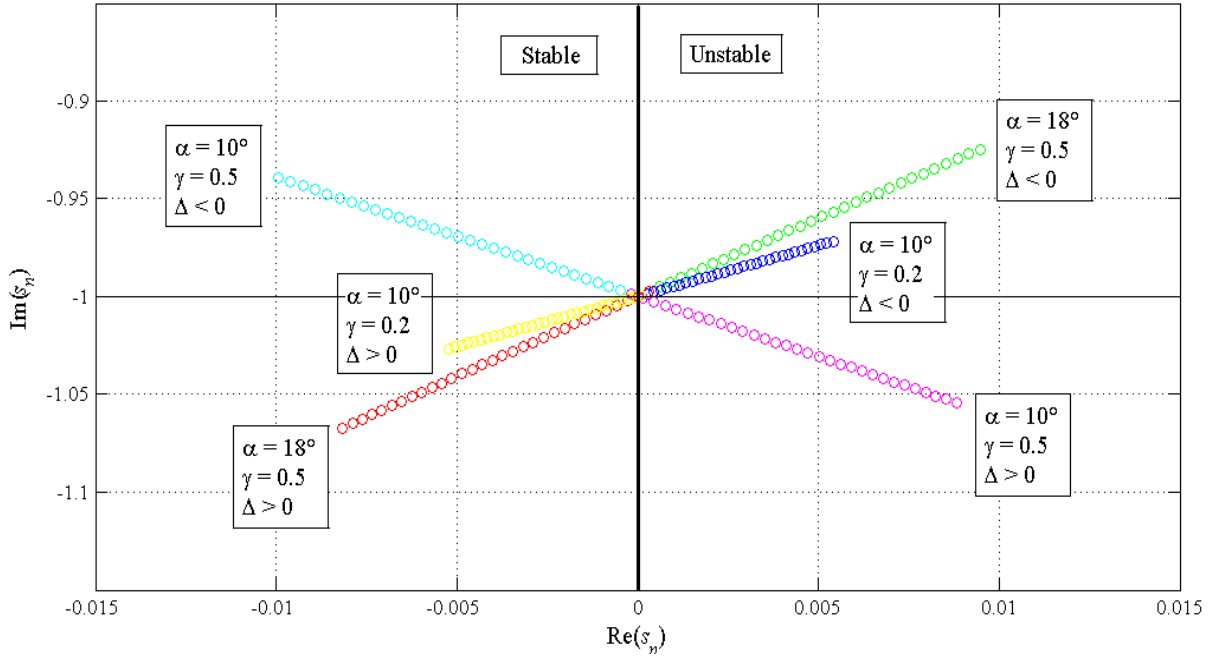


Fig. 3.2: Root loci for one of the eigenvalues of the vertical mode ($\zeta = 0$).

A scenario of the effects of parameters α , γ , ζ and Δ on the dynamic behaviour of the model can be observed on stability maps, computed by applying again the Hurwitz criterion. The maps shown in Figs. 3.3-3.6 are plotted as functions of the parameters α and γ (the latter being closely related with the relaxation length). Unstable regions are coloured, stable regions are white.

In the case of the model proposed by Pacejka [32], the unstable regions would have been limited to the lobes on the right-upper side of the plots. In these unstable areas both α and γ assume values which are non-realistic (i.e. excessive) for motorcycles: the regions of practical interest of the maps are their lower left portions.

When considering the interaction of the chain, however, unstable regions appear for lower values of α and γ , in proximity of the origin of the axes, and in the region of practical interest for motorcycles.

Figs. 3.3 – 3.5 are referred to the undamped system ($\zeta = 0$), showing the effect of changing the coupling parameter Δ from a small negative value to a small positive one: for values of α in the range of 10° to 18° , and for values of $(1 - \eta)\gamma$ in the range from 0.1 to 1, Figs. 3.3 and 3.4 show an opposite behaviour.

Fig. 3.5 shows the effect of suspension damping: the unstable regions rapidly vanish by increasing ζ , and the portion of practical interest for motorcycles results to be completely stable even for small values of ζ .

The effects of V_x and η are finally analyzed. An increase of V_x increases the damping, and therefore enlarges the stability regions. On the other hand η , which can vary from 0 to 1, when $\eta = 1$ the system is always stable; when $\eta = 0$ the unstable regions reach their largest extension (all of the other parameters hold fixed).

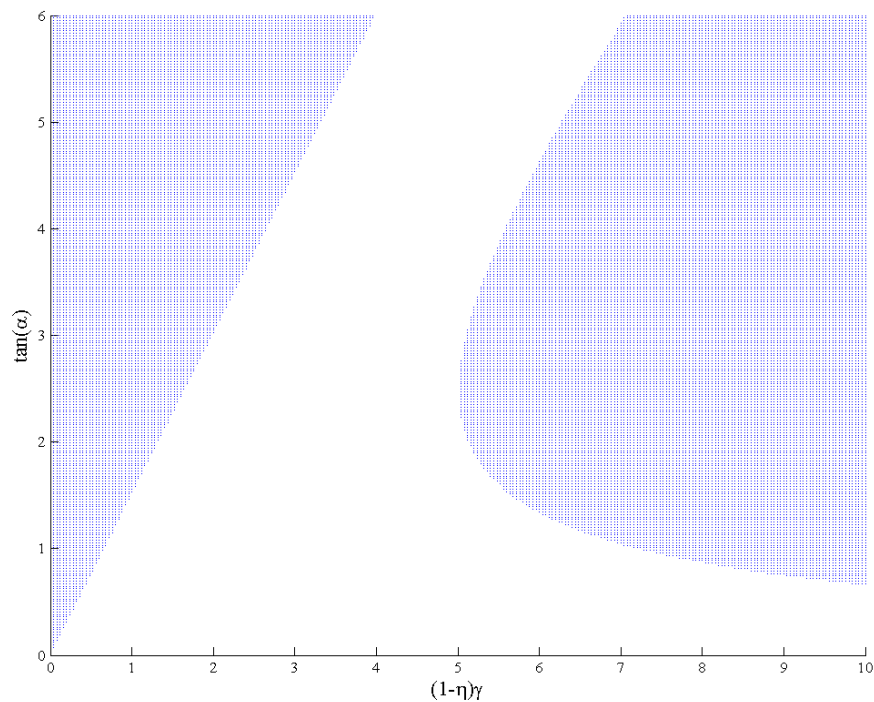


Fig. 3.3: Negative Δ ($\Delta = -0.02$), with $\zeta = 0$.

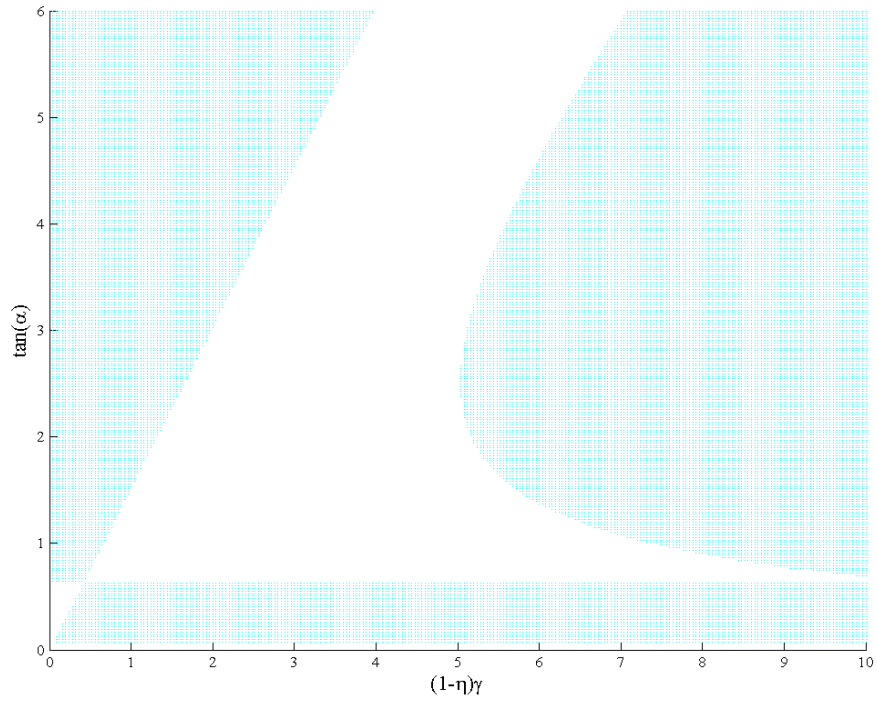


Fig. 3.4: Positive Δ ($\Delta = + 0.02$), with $\zeta = 0$.

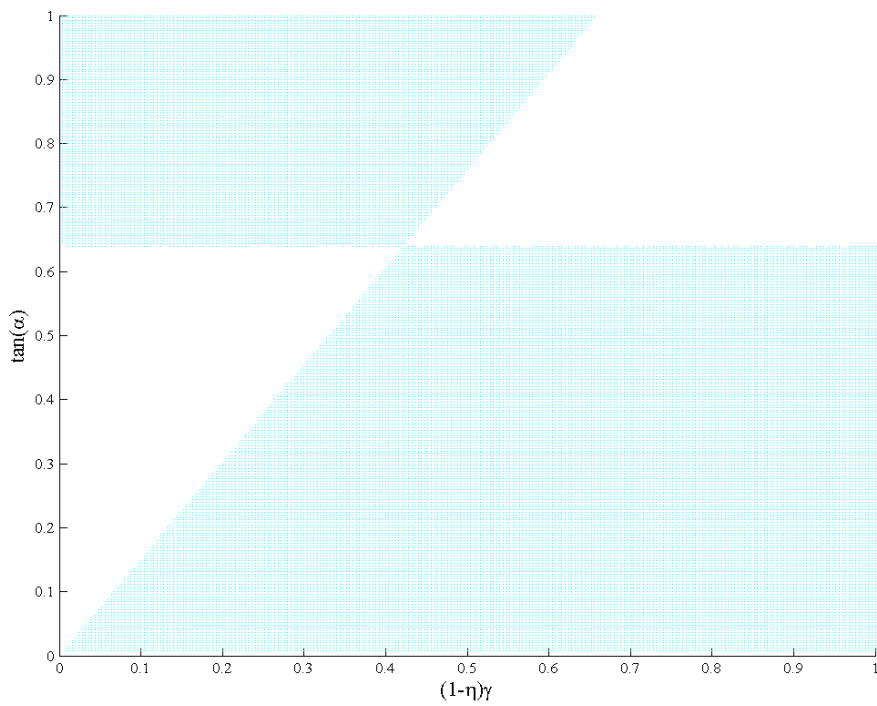


Fig. 3.5: Positive Δ ($\Delta = + 0.02$). Close-up view of Fig. 3.4.

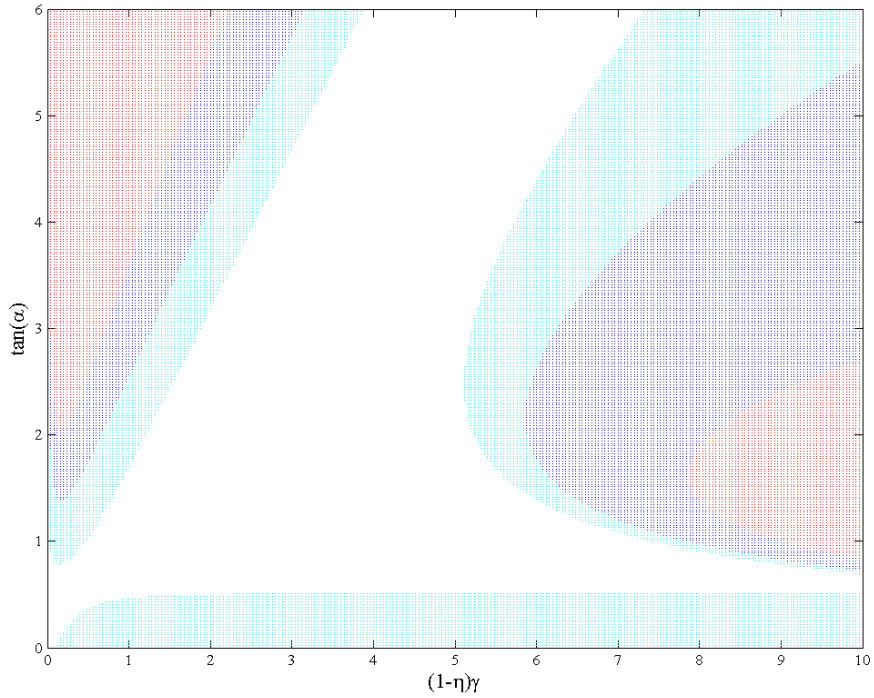


Fig. 3.6: Positive Δ ($\Delta = + 0.02$), with 3 different levels of damping

($\zeta = 0.001$ cyan, $\zeta = 0.01$ blue and $\zeta = 0.03$ red).

3.4 REMARKS ON SLIP MODELS

The expression of the longitudinal slip force F_x can be obtained from the constitutive equation of the Maxwell model (represented in the Fig. 3.7), consisting of a series of a spring (stiffness C_x) and a damper (damping coefficient C_k/V_x).

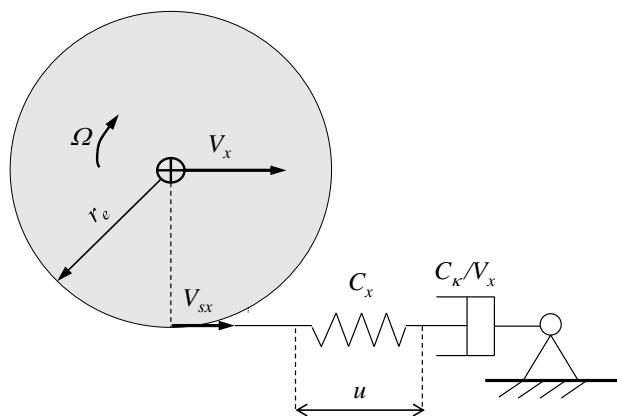


Fig. 3.7: Slip model as a Maxwell spring damper system.

The force acting on the spring is the same acting on the damper. As a consequence, the system behaviour is dominated by the spring at low speed, while the damper is dominant at high speed (since the damping coefficient is inversely proportional with respect to V_x).

The constitutive equation of the Maxwell model gives:

$$\frac{C_\kappa}{V_x} \dot{F}_x + C_x F_x = \frac{C_\kappa}{V_x} C_x (-V_{sx}) \quad (3.8)$$

which, divided by the stiffness coefficient, yields the standard formula:

$$\frac{\sigma_\kappa}{V_x} \dot{F}_x + F_x = -C_\kappa \frac{V_{sx}}{V_x} = C_\kappa \kappa \quad (3.9)$$

showing the dependency on the relaxation length σ_κ . The same equation can be rewritten in terms of the steady-state value of the longitudinal slip force (i.e. F_{xss}):

$$\sigma_\kappa \dot{F}_x + V_x F_x = V_x F_{xss} \quad (3.10)$$

or by taking into account the displacement u of the contact point:

$$\begin{cases} F_x = C_x u \\ u = \phi r_e \simeq \phi r_e \end{cases} \quad (3.11)$$

that is the very well-known form, also implemented in the multibody vehicle model (chapter 1):

$$\sigma_\kappa \dot{u} + V_x u = -\sigma_\kappa V_{sx} \quad (3.12)$$

These expressions are valid in general, for non-steady-state force F_x and velocity V_{sx} .

In the following some functions will be expressed by highlighting two separate contributions: one taking into account the steady state (nearly constant) value of the function (subscript 0) and one considering the oscillating, variable value of the function (symbol \sim).

The variable parts are assumed to be small, in order to linearize the equations. So, for example considering the longitudinal slip speed V_{sx} :

$$F_x = -\frac{C_\kappa}{V_x} (V_{sx0} + \tilde{V}_{sx}) \quad (3.13)$$

The expression of F_x adopted at the beginning of chapter 4 has been written (according to Pacejka [32]) assuming a constant value for C_κ (as well as a constant value for the relaxation length σ_κ) and neglecting the constant part of V_{sx} , giving:

$$F_x = \frac{C_\kappa}{V_x} \underbrace{\left[r(\Omega + \dot{\phi}) - \dot{x} - (1 - \eta) \frac{V_x}{r} z \right]}_{-\tilde{V}_{sx}} \quad (3.14)$$

where the expression in square brackets represents $-\tilde{V}_{sx}$. As already mentioned, the term which may cause instability is the factor $(1 - \eta)$.

As an alternative approach, a variable C_κ may be considered, linearly dependent on the vertical load F_z (as in chapter 4, Eq. 4.1)

$$C_\kappa = C_{\kappa0} + \tilde{C}_\kappa = C_{\kappa0} + \chi F_z \quad (3.15)$$

where χ is a proportionality constant. Setting $\eta = 1$ in \tilde{V}_{sx} and taking into account the constant part V_{sx0} gives an alternative expression for F_x :

$$\left. \begin{array}{l} C_\kappa = C_{\kappa0} + \tilde{C}_\kappa \\ \eta = 1 \\ V_{sx0} \neq 0 \end{array} \right\} \Rightarrow F_x = - \left(\frac{C_{\kappa0}}{V_x} \tilde{V}_{sx} \Big|_{\eta=1} + \frac{\tilde{C}_\kappa}{V_x} V_{sx0} \right) \quad (3.16)$$

where the non-linear term $\tilde{C}_\kappa \cdot \tilde{V}_{sx}$ was neglected.

Taking into account the linear dependency of the vertical load with respect to z :

$$\left. \begin{array}{l} F_z = C_z z \\ \tilde{C}_\kappa = \chi F_z \end{array} \right\} \Rightarrow \tilde{C}_\kappa = \lambda z \quad (3.17)$$

the expression of F_x becomes:

$$F_x = \frac{C_{\kappa 0}}{V_x} \left[r(\Omega + \dot{\phi}) - \dot{x} \right] - \lambda \frac{V_{sx0}}{V_x} z \quad (3.18)$$

which (assuming a constant value for C_x) yields immediately:

$$\left. \begin{array}{l} \dot{\phi} = -\frac{\dot{F}_x}{rC_x} \\ \Lambda = \lambda \frac{V_{sx0}}{V_x} \end{array} \right\} \Rightarrow \frac{\sigma_{\kappa 0}}{V_x} \dot{F}_x + F_x = \frac{C_{\kappa 0}}{V_x} (r\Omega - \dot{x}) - \Lambda z \quad (3.19)$$

This constitutive equation for F_x closely resembles the one employed at the beginning of this chapter, the only difference being the constant of linear proportionality to the vertical displacement z . Therefore the two constitutive models are perfectly equivalent if the following condition is satisfied:

$$\Lambda = (1-\eta) \frac{C_{\kappa 0}}{r} \Rightarrow \chi = (1-\eta) \frac{C_{\kappa 0}}{rC_z} \frac{V_x}{V_{sx0}} \quad (3.20)$$

If $\eta \rightarrow 1$, then $\Lambda \rightarrow 0$ and $\chi \rightarrow 0$: in any case the model becomes stable.

3.5 CONCLUSIONS

A simplified linear model of the motorcycle rear wheel with suspension and chain transmission was developed, based on a classical study of the self-excited wheel hop. A stability analysis of the model was carried out, showing the major influences of chain force and suspension damping. By means of further analytical developments it was demonstrated that the relaxation model adopted in [31] (with relaxation length linearly dependent on vertical load) is equivalent to the slip model presented in the literature in order to explain the self-excited wheel hop.

Chapter 4

THE CHATTERING VIBRATION OF RACING MOTORCYCLES

4.1 INTRODUCTION

The chatter phenomenon, appearing during high speed cornering maneuvers performed by racing motorcycles, consists of a self-excited vertical oscillation of both the front and rear unsprung masses in the range of frequency between 17 and 22 Hz. The suspensions are not generally able to dampen the above vibrations which start from the rear wheel and suddenly propagate to the front wheel during the corner entry phase, making the vehicle's handling unpredictable and, ultimately, weakening the overall performance, that is the lap time. The determining factor causing this phenomenon is still not clear.

The chattering is perceived by the rider as a severe vertical vibration appearing in particular sections of the track. Namely, riders experience chattering during the latter phase of corner entry, while exerting high front brake torque and engine brake torque at high lean angle. The vibration continues during the rolling phase throughout the corner apex up to the corner exit. The vibration quickly disappears while accelerating out of the corner. During chattering the confidence of the rider drops down because it becomes more difficult to estimate the tire adherence which is still available, preventing him from obtaining the maximum possible longitudinal and lateral acceleration. Therefore performance during braking and turning is seriously affected by this phenomenon, and the risk of crashing is increased. Several contributions to the understanding of this phenomenon have been published, highlighting different aspects. In 2004 Tezuka et al. [33] showed how an unstable mode due to the lateral and longitudinal deformability of the tires may appear when increasing the cornering effort, but they did not consider the effects of braking and of the engine drivetrain inertia. In 2008 Cossalter et al. [34] demonstrated that a self-excited vibration shows up during a straight-running braking maneuver, due to the interaction between transmission and tires, neglecting the effects of roll. In 2013 Sharp [35] found that the lateral and torsional flexibilities of the frame may take part in the phenomenon during a steady state cornering maneuver, but, again, the presence of braking forces was neglected. This demonstrates how the phenomenon is far from being understood.

Aim of this chapter is to simulate the actual vibration, highlighting its driving mechanism and which components of the motorcycle are involved [36]. To this purpose, the comprehensive motorcycle model described in chapter 1 will be used to simulate a three dimensional maneuver experimentally measured on the race track, for a Ducati MotoGP class vehicle.

4.2 PARAMETER ESTIMATION

In order to perform accurate dynamic simulations, an experimental estimate of the model parameters introduced with the rigid-ring model is required. For this purpose a road racing motorcycle was tested using a two-post test rig. Its setup features two hydraulic actuators (controlled in closed loop) exciting the actual vehicle at the wheel contact points. The imposed ground displacement can be calculated as shown in chapter 2. The system response was measured by means of two tri-axial accelerometers fixed on the wheel spindles as shown in Fig. 4.1.

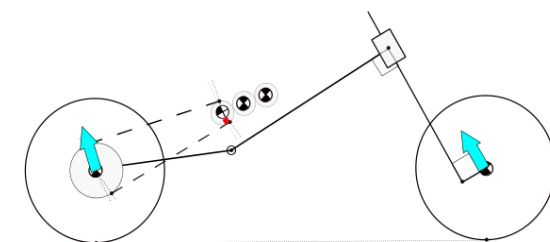


Fig. 4.1: Z-axis position and orientation for the accelerometers fixed on the wheel spindles.

This experimental setup made it possible to update the model parameters by means of fitting the experimental data. Fig. 4.2 shows a comparison between experimental (red lines) and simulated (black lines) frequency response functions, for three configurations of interest. The figure axes are dimensionless for confidentiality purpose. The first one (dashed line) is the ratio between the Fourier transforms of the Z signal of the rear spindle accelerometer and the signal of the load cell at the rear contact point. The second one (solid line) is the ratio between the Fourier transforms of the Z signal of the front spindle accelerometer and the signal of the load cell at the front contact point. The third one (dotted line) is the ratio between the Fourier transforms of the X (forward) signal of the front spindle accelerometer and the signal of the load cell at the front contact point. It is possible to notice a peak for the first two signals at nearly the same frequency, corresponding to the natural frequency of the front and rear tire radial deformation. This made it possible an accurate tuning of the rigid-ring stiffness by fitting the experimental data. Consequently, the residual stiffness could be computed according to Eq. (1.9) in order to ensure the actual overall tire deformability. The same procedure can be adopted for the lateral stiffness. The third signal shows a peak at a much higher frequency, corresponding to the first in-plane frame flexional mode. Through the front telescopic fork this mode is visible at the front wheel spindle.

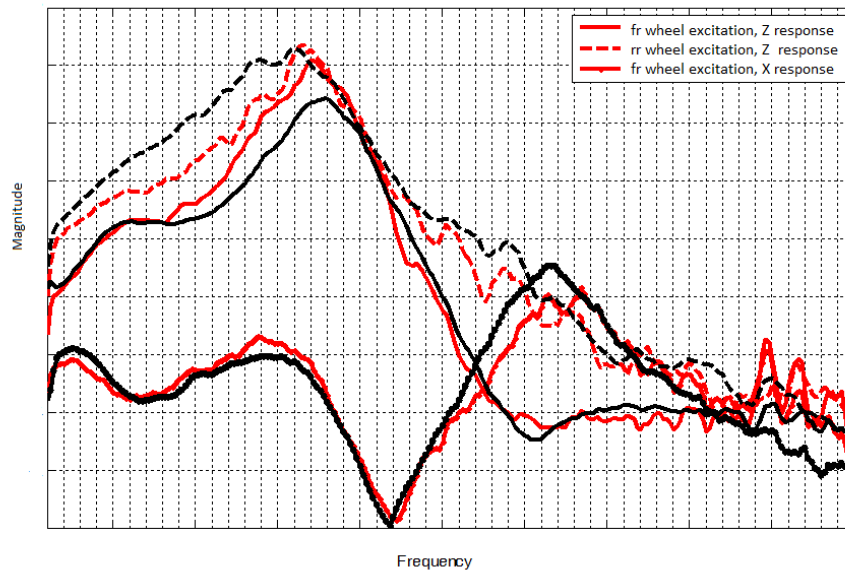


Fig. 4.2: Experimental (red) and simulated (black) frequency response of the whole motorcycle.

4.3 MANEUVER DESCRIPTION

In this section some experimental evidences of chattering are shown. The data have been recorded via a telemetric system installed on the motorcycle, during a lap of Sepang international racetrack. The critical maneuver considered includes the turns T12, T13 and T14 of the track, as shown in Fig. 4.3, and it consists of a lean angle braking phase followed by high roll angle cornering and acceleration as shown in Fig. 4.4.

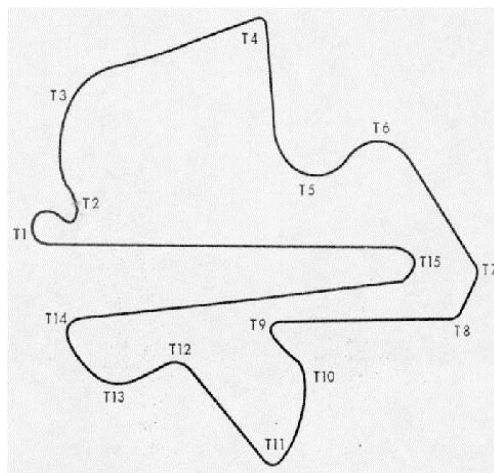


Fig. 4.3: Sepang racetrack layout, counterclockwise direction.

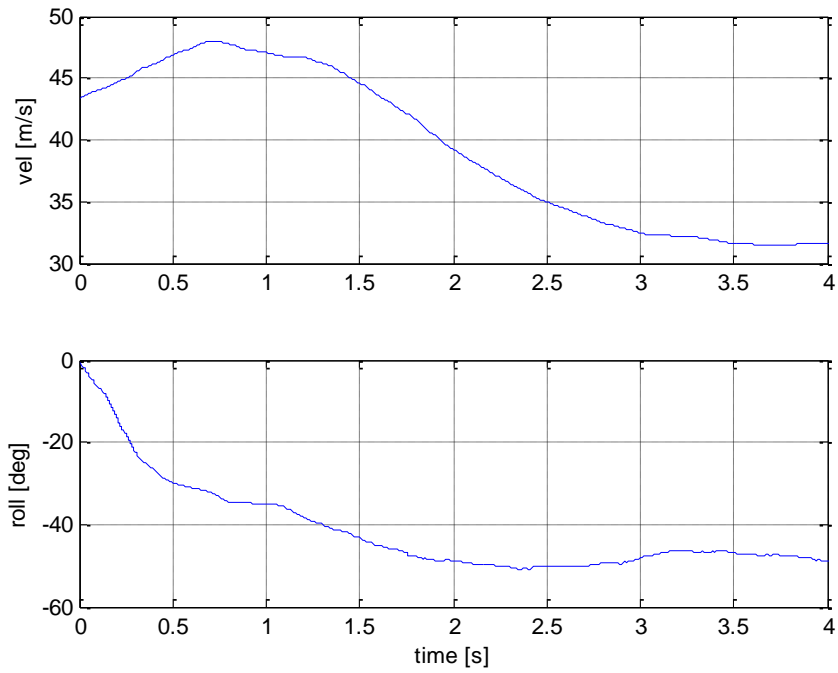


Fig. 4.4: Measured speed and roll profiles.

The braking is performed with front brake and engine brake up to a roll angle of 55° as shown in Fig. 4.5. Note that all data were normalized with respect to their maximum values for confidentiality reasons.

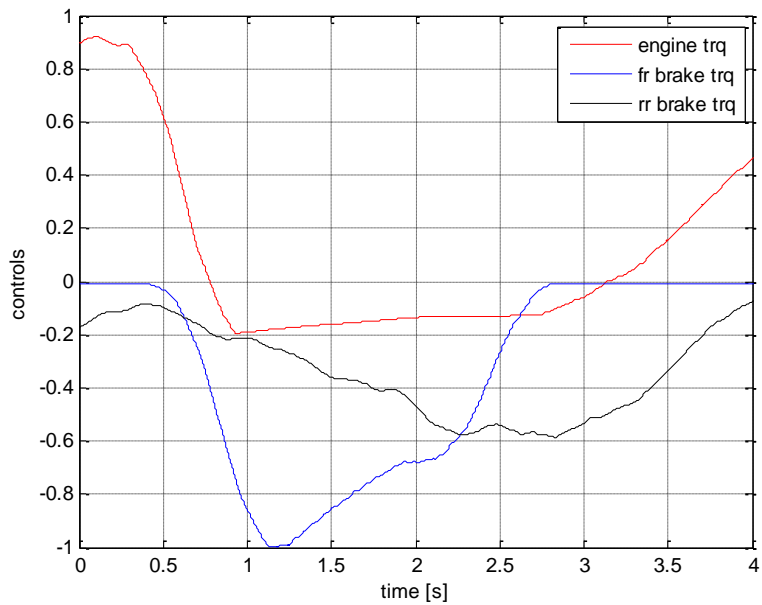


Fig. 4.5: Measured torques requested by the rider.

The engine and front brake torques are calculated from the inputs given by the rider: throttle angle and brake circuit pressure. During the subsequent very short cornering phase, low engine and rear brake torques are applied, limited by the engine's idle speed and anti-hop clutch. Then engine torque is gradually increased by the rider up to the maximum available. Figure 4.6 shows the signals in vertical direction of two accelerometers rigidly connected with the wheels spindles as shown in Fig. 4.1.

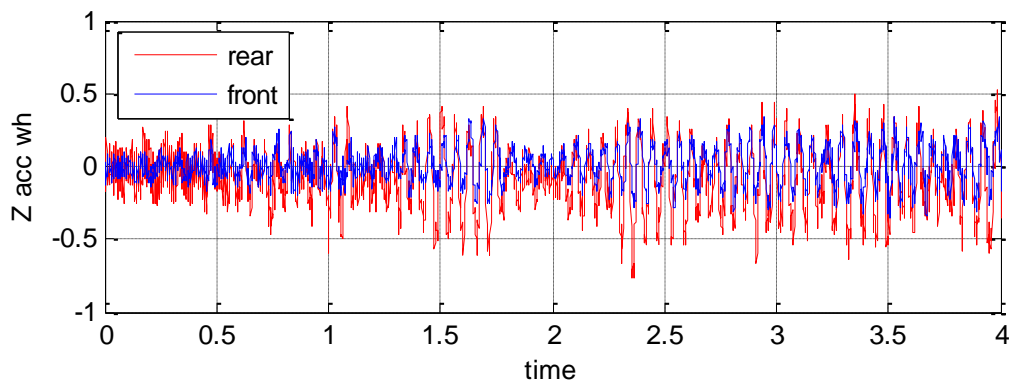


Fig. 4.6: Normalized vertical acceleration of the wheel spindles.

A chatter phenomenon is evident, and the measured vertical acceleration of both axles are in the range of magnitude of tens of m/s^2 . This leads to a great fluctuation of the vertical load acting on the tires. As it is very well known, a strongly nonlinear function correlates vertical tire load, slip and camber angles to longitudinal and lateral ground forces, and a high fluctuation of the driving forces of the tires is expected, yielding the unpredictable behaviour of the motorcycle which riders complain about.

4.4 MODEL LINEARIZATION

This section deals with the stability of the motorcycle in particular configurations extracted from the above described maneuver. To simulate this maneuver, proper controllers were implemented in the model: a longitudinal PI controller for imposing a velocity profile, along with a PID steering controller for ensuring the equilibrium at the desired roll angle. The linear response of the model was evaluated with a numerical perturbation routine. In order to highlight the dependence of the longitudinal relaxation length from the vertical load the definition of relaxation length given in Eq. (1.18) was replaced with an explicitly linear one, as follows:

$$\sigma_{\kappa} = p \cdot R_0 \cdot \frac{F_N}{F_{N0}} \quad (4.1)$$

where R_0 is the undeformed rear tire radius and F_{N0} is a reference vertical load as defined in [4]. The influence of the slope p in Eq. (4.1) is first investigated, for both front and rear relaxation lengths. A straight running maneuver at $\dot{x} = 45 \text{ m/s}$, is considered, with $p \in \{0.5, 0.75, 1, 1.25, 1.5, 2\}$. Fig. 4.7 shows the root locus, i.e. the eigenvalues of the system, computed for the 6 different values of p , neglecting those related to the steering motions (weave, wobble) for the sake of clarity. The suspension damping was weakened in order to highlight the contribution of the rigid-ring tire model. The eigenvalues corresponding to the parameter $p = 2$ are marked with a star.

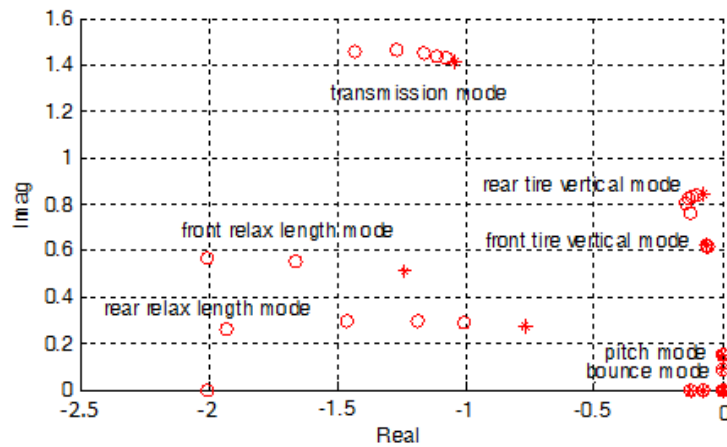


Fig. 4.7: Root locus, straight running maneuver.

Figure 4.7 shows the eigenvalues corresponding to 7 natural modes:

- 1) Bounce mode: vertical oscillation of the sprung mass, which shows very poor stability due to the reduction in suspension damping,
- 2) Pitch mode: angular oscillation in the motorcycle midplane of the sprung mass (counterphase compression of the suspensions); weak stability due to the reduction in suspension damping,
- 3) Front tire vertical mode: vertical oscillation of the front tire belt with respect to the rim,
- 4) Rear tire vertical mode: vertical oscillation of the rear tire belt with respect to the rim,
- 5) Transmission mode: angular oscillation of the gearbox shafts and crankshaft,
- 6) Front relaxation length mode: angular oscillation of the entire front tire with respect to the ground,
- 7) Rear relaxation length mode: angular oscillation of the entire rear tire with respect to the ground.

It can be observed that by increasing the values of p , the stability of the rear tire vertical mode is weakened, and the same occurs with respect to relaxation length modes.

The effects of deceleration and braking style during cornering are now investigated, assuming a realistic value of the parameter $p = 0.5$. Linear velocity profiles with constant acceleration values $a \in -\{0, 2, 4, 6, 8\} m/s^2$ and final velocity $\dot{x} = 40 m/s$ with a roll angle $\varphi = 50^\circ$ were obtained with the front brake only, resulting in a loss of stability of the front tire vertical mode, with minor effects on the rear tire (Fig. 4.8). Moreover, the front relaxation length mode become stable for all the decelerations tested. The pitch mode is affected as well, becoming unstable.

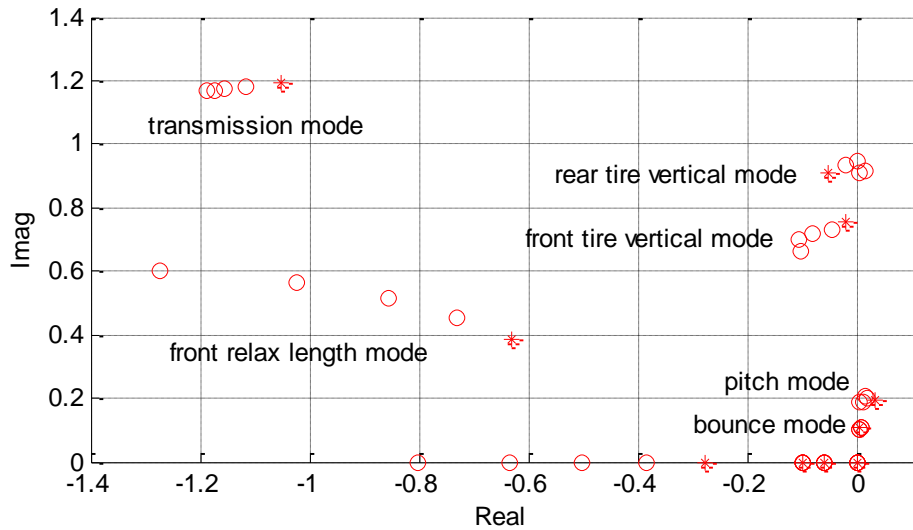


Fig. 4.8: Root locus, front braking maneuver.

On the other hand, when the same maneuver is obtained with a realistic brake distribution at the rear wheel, such as 60% front brake, 20% engine brake and 20% rear brake, the rear tire vertical mode becomes clearly unstable, and a greater participation of the transmission mode is evident, as shown in Fig. 4.9.

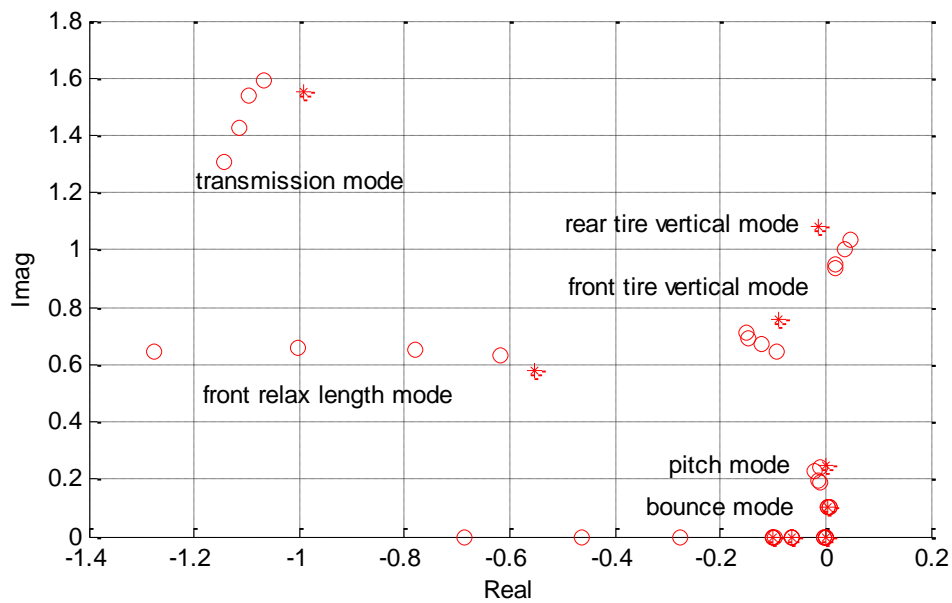


Fig. 4.9: Root locus, combined braking maneuver.

4.5 MANEUVER SIMULATION

The reference maneuver was simulated with the full model developed in chapter 1, in order to highlight unstable motions of the system. A PID steering controller was implemented to reproduce the measured roll profile, while the other controls, i.e. engine torque, front and rear brake torques, were imposed in open loop. A low pass filter was first applied to the measured input signals, in order to eliminate high frequency components. The integration was carried out with a multistep solver available in Matlab environment (ODE15s). Note that no road elevation was considered. The velocity and roll profiles are presented in Fig. 4.10 with respect to the experimental data, showing the consistency of the simulated maneuver. A difference in the initial condition is introduced in order to compensate for the actual vehicle acceleration at the initial point.

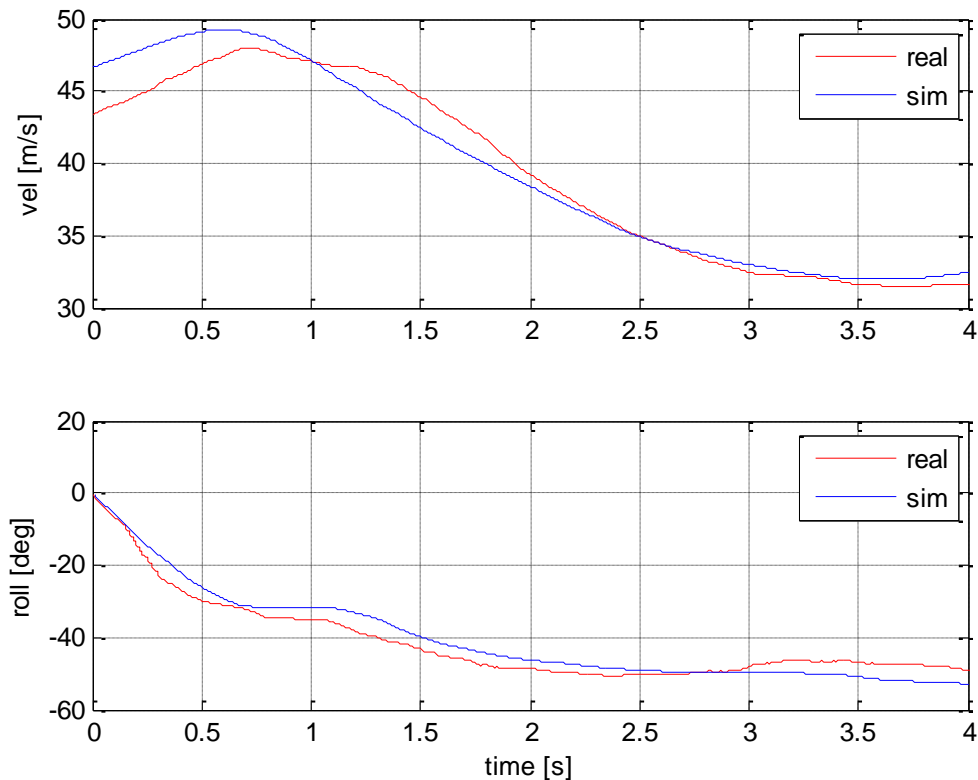


Fig. 4.10: Measured vs simulated speed and roll profiles.

The vertical load acting on the contact points (Fig. 4.11), oscillates at around 18 Hz, its oscillation starting at 2 s from the rear, and then propagating at 2.5 s to the front. Its

amplitude is larger at the rear, according to linear analysis. This vibration quickly vanishes as a positive engine torque is applied starting at 3.5 s. The actual vertical ground forces were computed through the data recorded by the Inertial Measuring Unit (IMU) installed on the motorbike.

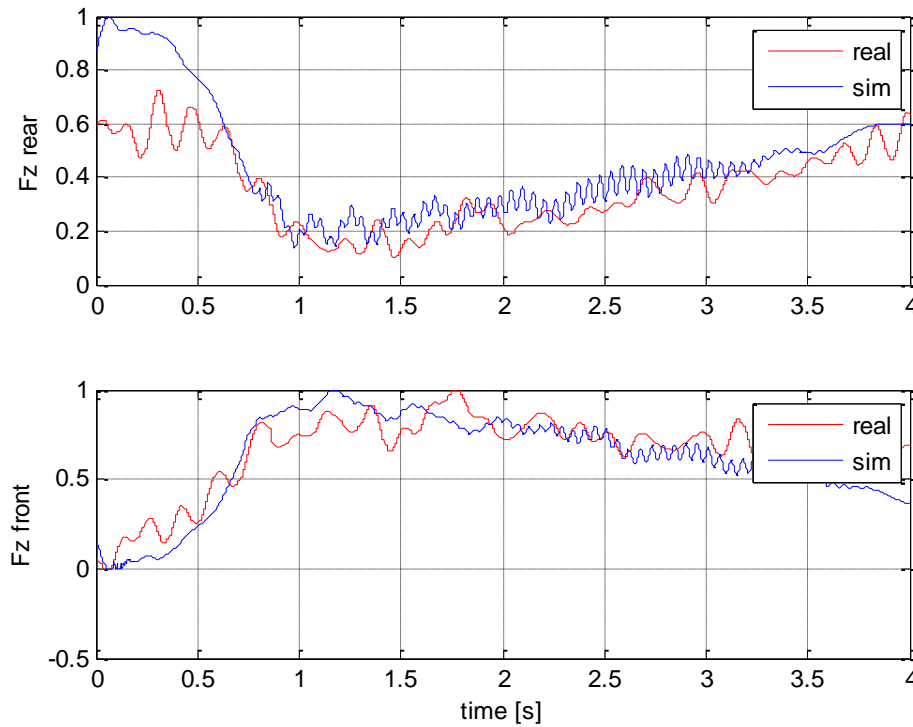


Fig. 4.11: Measured vs simulated vertical wheel loads.

A vibration at the same frequency is also present in the suspension strokes (Fig. 4.12). It can be noticed that this vibration takes place around a mean value which is far from the static suspension stroke for both the suspensions, due to the in-plane component of inertial forces related to roll. Accordingly to the actual chatter features, this vibration starts from the rear and then propagates to the front, but with lower intensity.

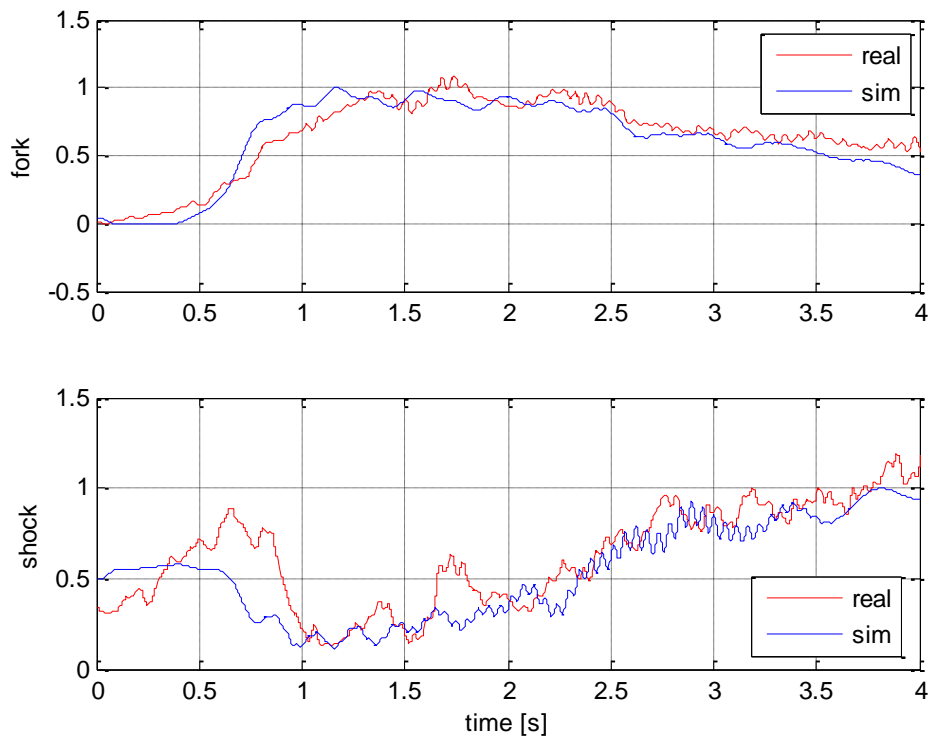


Fig. 4.12: Measured vs simulated suspension strokes.

A better gauge for chattering vibration is the vertical acceleration of the wheel spindles, as reported in Fig. 4.13. The graph shows that the simulated vertical accelerations of the axles start from the rear with greater magnitude and, again, it propagates to the front, with the same frequency, resulting in a pitching motion of the entire motorcycle (as a rigid body) over the tires deformability.

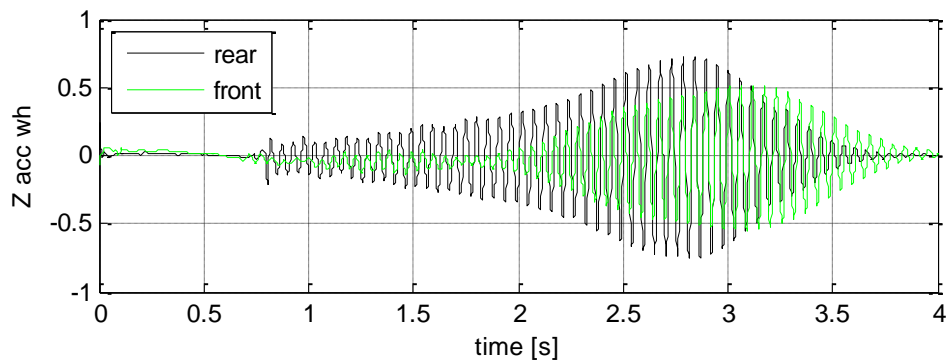


Fig. 4.13: Simulated wheel spindle acceleration.

A close up of measured vs simulated spindle accelerations is reported in Fig. 4.14, showing a satisfactory global agreement, in terms of both amplitudes and frequencies.

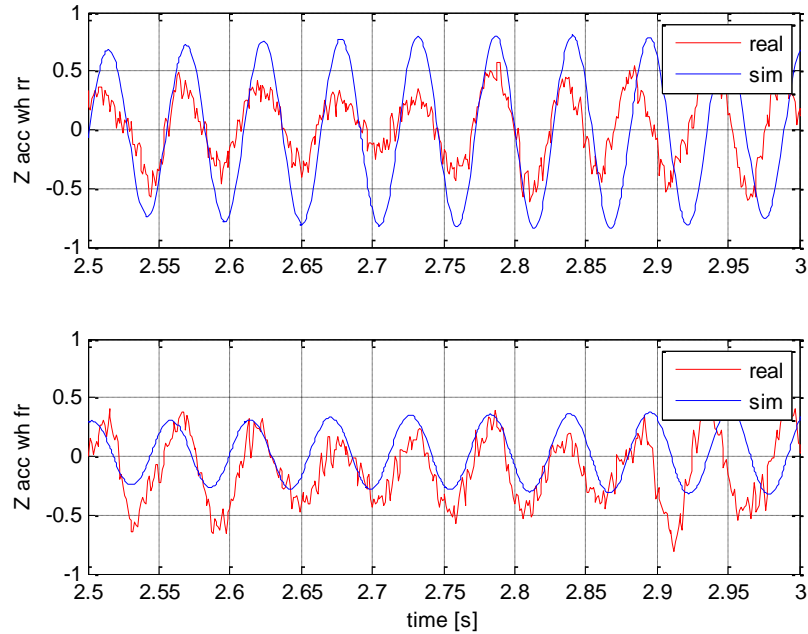


Fig. 4.14: Measured vs simulated wheel spindle accelerations.

4.6 CONCLUSIONS

The crucial factor leading to the chattering vibration is the dependency of longitudinal relaxation length from vertical load. To prove this, the maneuver was simulated again with a constant equivalent relaxation length, and the resulting vibrations were compared to the previously obtained ones, as shown in Fig. 4.15. The graphs marked in red are those obtained with the load dependent relaxation length, while the graphs marked in blue are those obtained in the case of constant relaxation length.

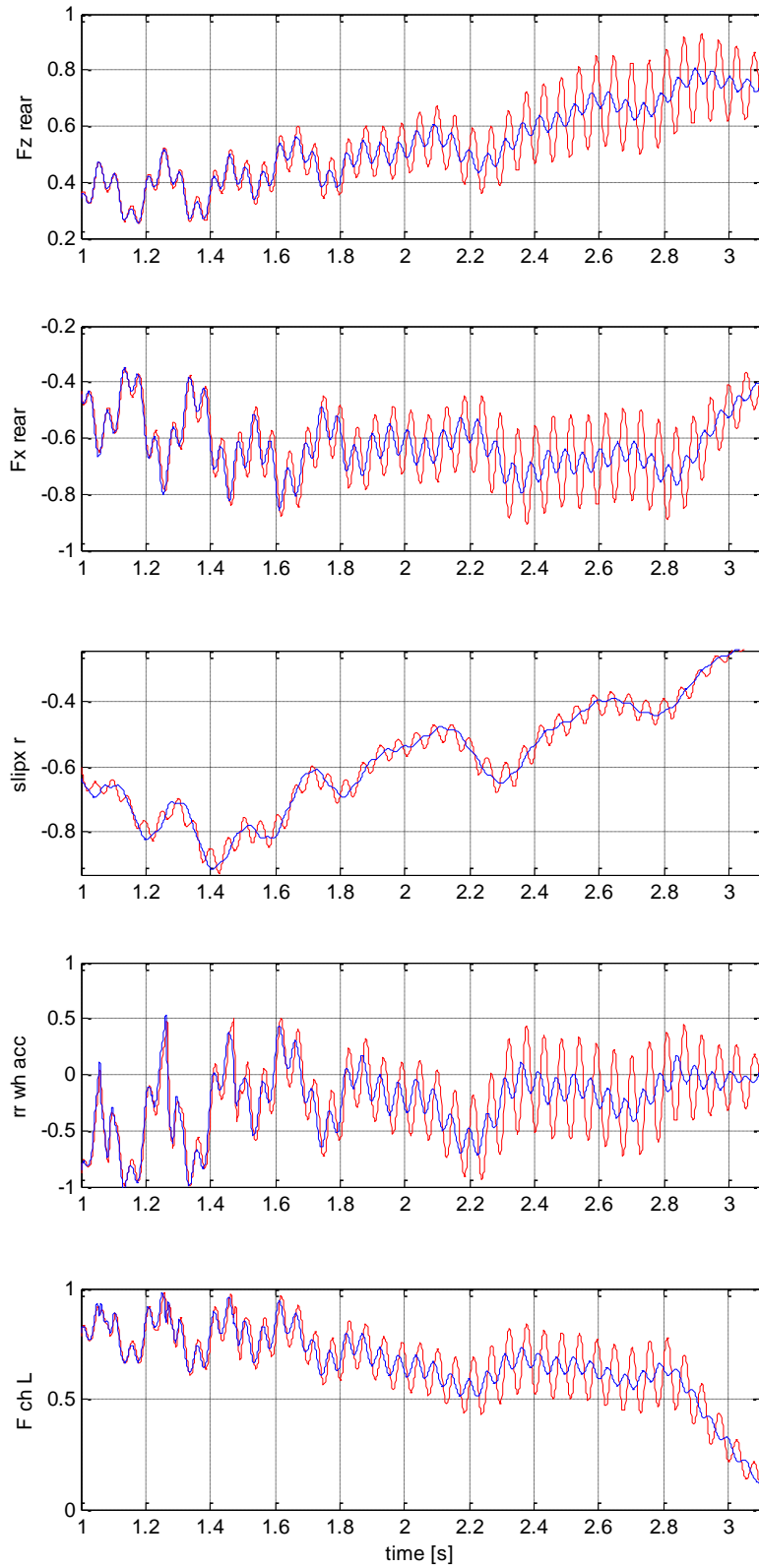


Fig. 4.15: Comparison between non chattering (blue) and chattering (red) simulations.

Figure 4.15 shows respectively:

- 1) vertical load acting on the rear contact point,
- 2) rear tire-ground longitudinal force (negative when braking),
- 3) rear wheel longitudinal slip,
- 4) rear wheel absolute angular acceleration (negative when decelerating),
- 5) chain force in the lower segment (positive when decelerating the wheel).

In conclusion, the following physical interpretation of the chatter phenomenon is proposed: when a front and rear braking torque is applied, a transient starts, in which the rear tire vertical deformation mode is excited, due to the low damping of the tire carcass. This causes a fluctuation in the vertical load acting on the contact patch. When the relaxation length is kept constant this does not affect slip, the phase lag introduced between the longitudinal and vertical tire forces is nearly constant, and the vibration vanishes. On the other hand, when the relaxation length depends on vertical load, a fluctuation of slip starts along with tire deformation, introducing a fluctuating phase lag between vertical load and thrust. This generates a major oscillation in the rear wheel angular acceleration which is in phase with vertical load and in counter-phase with thrust. The rear wheel acceleration produces an increase in lower chain force, which compresses the suspension, increasing the vertical load, thus feeding the self-excited cycle. The front wheel receives the vibration from the rear wheel and it reacts in resonance, being the front tire natural frequencies close to the rear one as shown by linear analysis. The resulting vibration of the vehicle is an angular oscillation of the sprung mass, driven by the anti-phase tire vertical deformations.

REFERENCES

- [1] V. Cossalter and R. Lot. A motorcycle multi-body model for real time simulations based on the natural coordinates approach, *Vehicle System Dynamics* 37 (6), 2002: 423-447.
- [2] R.S. Sharp and D.J.N. Limebeer. A motorcycle model for stability and control analysis, *Multibody System Dynamics* 6 (2), 2001: 123-142.
- [3] R.S. Sharp, S. Evangelou and D.J.N. Limebeer. Advances in the modelling of motorcycle dynamics, *Multibody System Dynamics* 12, 2004:251-283.
- [4] H.B. Pacejka. *Tire and Vehicle Dynamics*, Butterworth-Heinemann, Oxford, 2002.
- [5] E.J.H. De Vries and H.B. Pacejka. The effect of tire modelling on the stability analysis of a motorcycle, in: *Proceedings of AVEC 1998*, Nagoya, 1998.
- [6] A.J.C. Schmeitz, S.T.H. Jansen, Y. Tezuka, M. Hasegawa and S. Miyagishi. Application of the rigid ring model for simulating the dynamics of motorcycle tyres on uneven roads, in: *Proceedings of the Bicycle and Motorcycle Dynamics 2010 Symposium on the Dynamics and Control of Single Track Vehicles*, Delft, 2010.
- [7] B.A.J. de Jong. Development and validation of the MC-Swift concept tire model, Master Thesis, Eindhoven University of Technology, Eindhoven, 2007.
- [8] I.J.M. Besselink, H.B. Pacejka, A.J.C. Schmeitz, and S.T.H. Jansen. The swift tyre model: overview and applications, in: *Proceedings of AVEC 2004*, Arnhem, 2004.
- [9] A. Saccon and J. Hauser. An efficient Newton method for general motorcycle kinematics, *Vehicle System Dynamics* 47(2), 2009: 221-241.
- [10] P.W.A. Zegelaar. The dynamic response of tyres to brake torque variations and road unevennesses, PhD thesis, Delft University of Technology, 1998.

- [11] A.J.C. Schmeitz. A semi-empirical three-dimensional model of the pneumatic tyre rolling over arbitrary uneven road surfaces, PhD thesis, Delft University of Technology, 2004.
- [12] E.J.H. de Vries and H.B. Pacejka. Motorcycle tyre measurements and models, *Vehicle System Dynamics* 29 (1), 1998: 280-298.
- [13] R. Lot and M. Da Lio. A symbolic approach for automatic generation of the equations of motion of multibody systems, *Multibody System Dynamics* 12, 2004: 147-172.
- [14] J. García de Jalón and E. Bayo. Kinematic and dynamic simulation of multibody systems, *The real time challenge*, Springer-Verlag, New York, 1994.
- [15] W. Schielen. Multibody system dynamics: roots and perspectives, *Multibody System Dynamics* 1, 1997: 149-188.
- [16] M. Arnold, B. Burgermeister, C. Führer, G. Hippmann and G. Rill. Numerical methods in vehicle system dynamics: state of the art and current developments, *Vehicle System Dynamics* 49 (7), 2011: 1159-1207.
- [17] M.A. Serna, R. Avilés and J. García de Jalón. Dynamic analysis of plane mechanisms with lower pairs in basic coordinates, *Mechanism and Machine Theory* 17, 1982: 397-403.
- [18] R. Von Schwerin. *Multibody System Simulation: Numerical Methods, Algorithms, and Software*, Springer-Verlag, 1999.
- [19] V. Cossalter. *Cinematica e dinamica della motocicletta*, Edizioni Progetto, Padova, 1999.
- [20] W. Schielen and B. Hu. Spectral simulation and shock absorber identification, *International Journal of Non-Linear Mechanics* 38, 2003: 161-171.

- [21] L. Segel and H.H. Lang. The mechanics of automotive hydraulic dampers at high stroking frequencies, in: Proceedings of 7th IAVSD Symposium on the Dynamics of Vehicle on Roads and on Railway Tracks, Cambridge, 1981: 192-214.
- [22] G. Genta and A. Campanile. An approximated approach to the study of motor vehicle suspensions with nonlinear shock absorbers, *Meccanica* 24, 1989: 47-57.
- [23] L. Leonelli and N. Mancinelli. An automated procedure for the optimization of suspension damping of road racing motorcycles, in: Proc. of the ASME 2013 International Mechanical Engineering Congress & Exposition IMECE2013, San Diego, USA, 2013.
- [24] G. Farin. Curves and surfaces for CAGD, Morgan Kaufmann - Academic Press, San Francisco - London, 2002.
- [25] P.W. Gaffney and M.J.D. Powell. Optimal interpolation, in: G.A. Watson, Numerical Analysis, Lecture Notes in Mathematics 506, 1976.
- [26] G.E. Forsythe and C.B. Moler. Computer solution of linear algebraic system, Prentice-Hall, Englewood Cliffs, 1967.
- [27] M. Mitschke. Dynamic der Kraftfahrzeuge, Springer-Verlag, Berlin, 1984.
- [28] M. Shinozuka and G. Deodatis. Simulation of stochastic processes by spectral representation, *Applied Mechanics Review* 44, 1991: 191-204.
- [29] K. Popp and W. Schielen. Ground vehicle dynamics, Springer-Verlag, Berlin, 2010.
- [30] G. Catania, L. Leonelli, N. Mancinelli. Optimization of the suspension damping parameters of a sport motorcycle, in: Atti del XX Congresso AIMETA, Bologna, 2011.
- [31] G. Catania, L. Leonelli and N. Mancinelli. A multibody motorcycle model for the analysis and prediction of chatter vibration, in: Proc. of the ASME 2013 International Mechanical Engineering Congress & Exposition IMECE2013, San Diego, USA, 2013.

- [32] H.B. Pacejka. Some recent investigations into dynamics and frictional behaviour of pneumatic tires, in: *The physics of tire traction: theory and experiment*, H.F. Hays and A.L. Browne Editors, Springer-Verlag, New York, 1974: 257-279.
- [33] Y. Tezuka, S. Kokubu, Y. Shiomi and S. Kiyota. Vibration Characteristics Analysis in Vehicle Body Vertical Plane of Motorcycle during Turning, in: *Proceedings of JSAE Annual Congress*, Yokohama, 2004.
- [34] V. Cossalter, R. Lot and M. Massaro. The chattering of racing motorcycles, *Vehicle System Dynamics* 46 (4), 2008: 339-353.
- [35] R.S. Sharp and Y. Watanabe. Chatter vibration of high-performance motorcycles, *Vehicle System Dynamics* 51 (3), 2013: 393-404.
- [36] L. Leonelli. A multibody model for the analysis of self-excited vibrations of racing motorcycles, in: *Atti del convegno "Sesta giornata di studio Ettore Funaioli"*, Bologna, Italy, 2012: 269-283.